Silicon Photonics-Wireless Interface ICs for Micro-/Millimeter-Wave Fiber-Wireless Networks in Standard CMOS/BiCMOS Technology

Minsu Ko

The Graduate School

Yonsei University

Department of Electrical and Electronic Engineering

Silicon Photonics-Wireless Interface ICs for Micro-/Millimeter-Wave Fiber-Wireless Networks in Standard CMOS/BiCMOS Technology

by

Minsu Ko

A Dissertation

Submitted to the Department of Electrical and Electronic Engineering

and the Graduate School of Yonsei University

in partial fulfillment of the requirements for the degree of

Doctor of Philosophy

August 2013

This certifies that the dissertation of Minsu Ko is approved.

_____

Thesis Supervisor: Woo-Young Choi

_____

Sang-Kook Han

_____

Byung-Wook Min

_____

Jae-Young Kim

_____

Yaoming Sun

The Graduate School

Yonsei University

August 2013

Table of Contents

List of Figures and Tables

Abstract

Silicon Photonics-Wireless Interface ICs for Micro-/Millimeter-Wave Fiber-Wireless Networks in Standard CMOS/BiCMOS Technology

Minsu Ko

Dept. of Electrical and Electronic Engineering

The Graduate School

Yonsei University

Silicon photonics-wireless interface (PWI) ICs for low-cost remote antenna unit (RAU) in fiber-wireless network are investigated by utilizing 850-nm CMOS-compatible silicon avalanche photodetectors (APDs) realized with standard CMOS/BiCMOS technology without any design rule violation. Three types of silicon PWI ICs are developed according to target wireless application and optical distribution scheme, and they are a 5-GHz PWI IC for microwave RF-over-fiber RAU, a 60-GHz balanced subharmonic optoelectronic mixer (SHOEM) for

millimeter-wave IF-over-fiber RAU, and a 60-GHz PWI IC for millimeter-wave baseband-over-fiber RAU.

The 5-GHz PWI IC composed of an APD, a preamplifier, and a power amplifier (PA) is implemented with standard 180-nm CMOS technology. The APD is realized in P^+/N-well junction with the optical window of 10 μm × 10 μm and operates in an avalanche multiplication region with high reverse bias voltage. Its maximum DC responsivity and photodetection bandwidth are 7.09 A/W and 3.92 GHz. In order to optimize the circuit, DC, AC, and noise of the APD are characterized and its small-signal equivalent circuit model is developed. The following amplifier is optimized for the given APD by using simultaneous noise and impedance matching technique. The resulting peak transimpedance gain and minimum input circuit noise current are 79.9 dBΩ at 5.42 GHz and 7.3 pA/√Hz at 5.38 GHz, respectively. For verification of the PWI IC, data transmission in 5-GHz fiber-wireless downlink with 54-Mb/s 64 quadrature amplitude modulation (QAM) orthogonal frequency-division multiplexing 802.11 wireless local area network (WLAN) data is demonstrated with the minimum error vector magnitude (EVM) of 2.66% at the optical input power of –8 dBm.

The balanced SHOEM fabricated with CMOS process layers in standard 250-nm SiGe BiCMOS technology is investigated for 60-GHz

IF-over-fiber RAU. The 60-GHz SHOEM converts optical IF signals into electrical 60-GHz signals directly with 30-GHz LO signals. For the balanced SHOEM, a pair of APDs is configured in a diode frequency doubler structure, and this improves the conversion efficiency 11 dB higher than a single-APD SHOEM. Two configurations for the balanced structure, which are common-N and common-P pairs, are compared for the device optimization. The common-N SHOEM shows 4 dB higher conversion efficiency and the common-P SHOEM has 1.74 times wider photodetection bandwidth. The SHOEM is demonstrated by 110-MHz 25-Mb/s 32QAM signal transmission in 60-GHz fiber-wireless downlink. The achieved minimum EVM is 2.4% at 30-GHz 12-dBm LO and 110-MHz 0-dBm optical IF signals.

The 60-GHz PWI IC, an integrated baseband photoreceiver and millimeter-wave transmitter, is developed in standard 250-nm SiGe BiCMOS technology. The PWI IC converts baseband optical data into 60-GHz binary phase-shift keying (BPSK) wireless data. The baseband photoreceiver consists of an APD, a transimpedance amplifier (TIA) with a DC-balanced buffer, and a variable-gain amplifier (VGA) having the gain range from –10 dB to 10 dB. It has the variable transimpedance gain from 58 to 78 dBΩ with the bandwidth over 2.57 GHz. The input-referred circuit noise current is 0.317 μA_{rms}. The 60-

GHz transmitter is composed of a 60-GHz double-balanced Gilbert-cell mixer as a BPSK modulator and a 60-GHz PA. The peak voltage conversion gain is 15.8 dB at 55-GHz LO, and the IF bandwidth is over 6 GHz. The output 1-dB compression point is 9.5 dBm. 2-m wireless transmission of 1.6-Gb/s broadband data in 60-GHz fiber-wireless network using the PWI IC is successfully demonstrated with the error-free operation achieved at −6-dBm optical input power.

Keywords: avalanche photodetector (APD), BiCMOS, binary phase-shift keying (BPSK), BPSK modulator, CMOS, fiber-wireless network, 5 GHz, low-noise amplifier (LNA), optoelectronics, photonics-wireless interface (PWI), photoreceiver, power amplifier (PA), preamplifier, remote antenna unit (RAU), silicon photonics, 60 GHz, subharmonic optoelectronic mixer (SHOEM), transimpedance amplifier (TIA), transmitter, variable-gain amplifier (VGA), wireless local area network (WLAN), wireless personal area network (WPAN)

1. Introduction

1-1. Fiber-Wireless Network

Since mobile communications have been one of the most important public services, there always has been a growing demand for faster data transfer and better mobility. Nowadays, especially after the great success of smartphones, the users are consuming a large amount of wireless data indoor and outdoor while using voice and video calls, watching HD streaming videos, listening streaming music, interacting with others in social network services. Most of the current wireless services mainly use microwave bands within a few GHz such as GSM, WiMAX, LTE, and Wi-Fi, but they are extending to millimeter-wave bands which enable Gb/s transmission such as 60-GHz wireless personal area network (WPAN) [1] and wireless local area network (WLAN) [2]. This leads an explosive increase of data capacity and a decrease of wireless coverage, and therefore fiber-wireless networks using optical fibers as a wired transmission medium have been preferred [3]–[10].

Fig. 1-1-1 shows the block diagram of fiber-wireless network. Optically modulated data are transmitted between a central office and

indoor and outdoor remote antenna units (RAUs) via fiber. RAU is one of the most important components, which is an interface between photonic and wireless domains. As shown in Fig. 1-1-2, RAU provides photonics-wireless interface (PWI) for both downlink and uplink, which consists of optoelectronic (O/E) and electrooptic (E/O) photonic devices and wireless devices. There are three possible schemes for optical data distribution; RF over fiber, IF over fiber, and baseband over fiber [3]. The RAU structure varies with the optical data distribution scheme. This will be discussed in the next section.

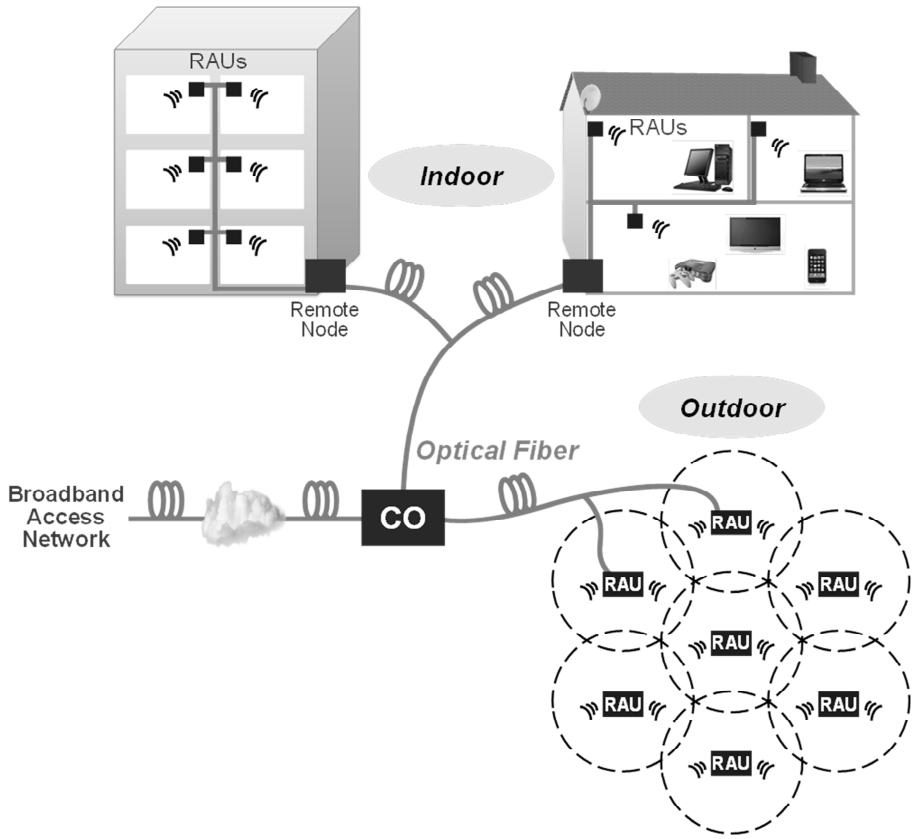

Fig. 1-1-1. Block diagram of fiber-wireless network.

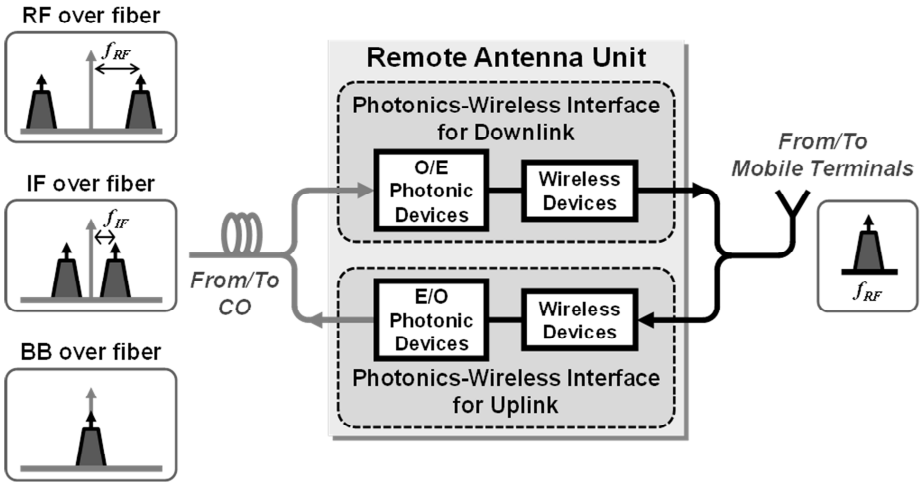

Fig. 1-1-2. Simplified block diagram of remote antenna unit. Optical data are distributed with three possible schemes; RF over fiber, IF over fiber, and baseband over fiber.

1-2. Low-Cost Silicon Integrated Remote Antenna Unit

The overall system cost of fiber-wireless network is dominated by RAU because a numerous number of RAUs are required per each CO. Over the last decade, there has been significant progress in silicon technologies, and silicon wireless devices for 60-GHz or higher bands can be realized with low-cost standard CMOS/BiCMOS technology [11]–[14]. On the other hand, silicon photonics has been actively investigated to develop photonic devices in silicon technology platform [15]–[19]. 1550-nm germanium photodetectors (PDs) on silicon substrate having the photodetection bandwidth as high as 42 GHz have been reported [16], [17]. Silicon E/O modulators (EOMs) which are Mach-Zehnder interferometer [18] or ring resonator [19] types with modulation bandwidth as high as 30 GHz also have been reported. By using silicon photonics technology, photonic devices and high-speed transistors can be integrated in a single silicon substrate. And, consequently, development of low-cost silicon integrated RAU including photonic and wireless devices can be also possible.

Fig. 1-2-1 shows block diagrams of silicon integrated RAUs consisting of PDs, EOMs, and electric circuits such as amplifiers, mixers, local oscillators (LOs), and digital circuits in a single chip. The

RF-over-fiber scheme shown in Fig. 1-2-1 (a) is the simplest for RAU implementation because frequency conversion is not required. Wireless network control is centralized at CO, so that wireless network can be reconfigured independent to RAU. However, the bandwidth of photonic devices should be high enough to handle RF signals. Optical data modulated in RF band are significantly affected by fiber chromatic dispersion, and it limits the optical transmission distance. On the other hand, the IF-over-fiber scheme shown in Fig. 1-2-1 (b) lessens the bandwidth requirement of photonic devices. Instead, wireless devices become more complex because up-/down-mixers and LOs are required for frequency conversion from or to the RF frequency. Alternately, the complexity can be relaxed by using O/E mixers [20], [21]. The O/E mixers detect optical IF signals and convert them into electrical RF signals by using nonlinearity of PDs. RAU is involved in wireless network control by IF-RF frequency conversion. The effect of fiber chromatic dispersion is greatly reduced. The block diagram of baseband-over-fiber RAU is shown in Fig. 1-2-1 (c). This type of RAU is the most complex because data modulation and demodulation should be done in RAU and consequently requires additional digital circuits. All the wireless network control functions should be done in RAU, but, at the same time, this scheme offers the best network flexibility by

separating MAC protocols of optical and wireless networks [10]. The chromatic dispersion effect is the least among three architectures. Comparison of three fiber-wireless network architectures is listed in Table 1-1.

The RAU structure available with silicon photonics technology is restricted by the RF frequency used in target wireless application because the currently developed photonic devices have not enough bandwidth to handle millimeter-wave bands over 30 GHz. Hence, for microwave applications such as LTE and Wi-Fi, all three structures are applicable, but RAUs for millimeter-wave application such as 60-GHz WPAN and WLAN can use only the IF-over-fiber and baseband-over-fiber structures.

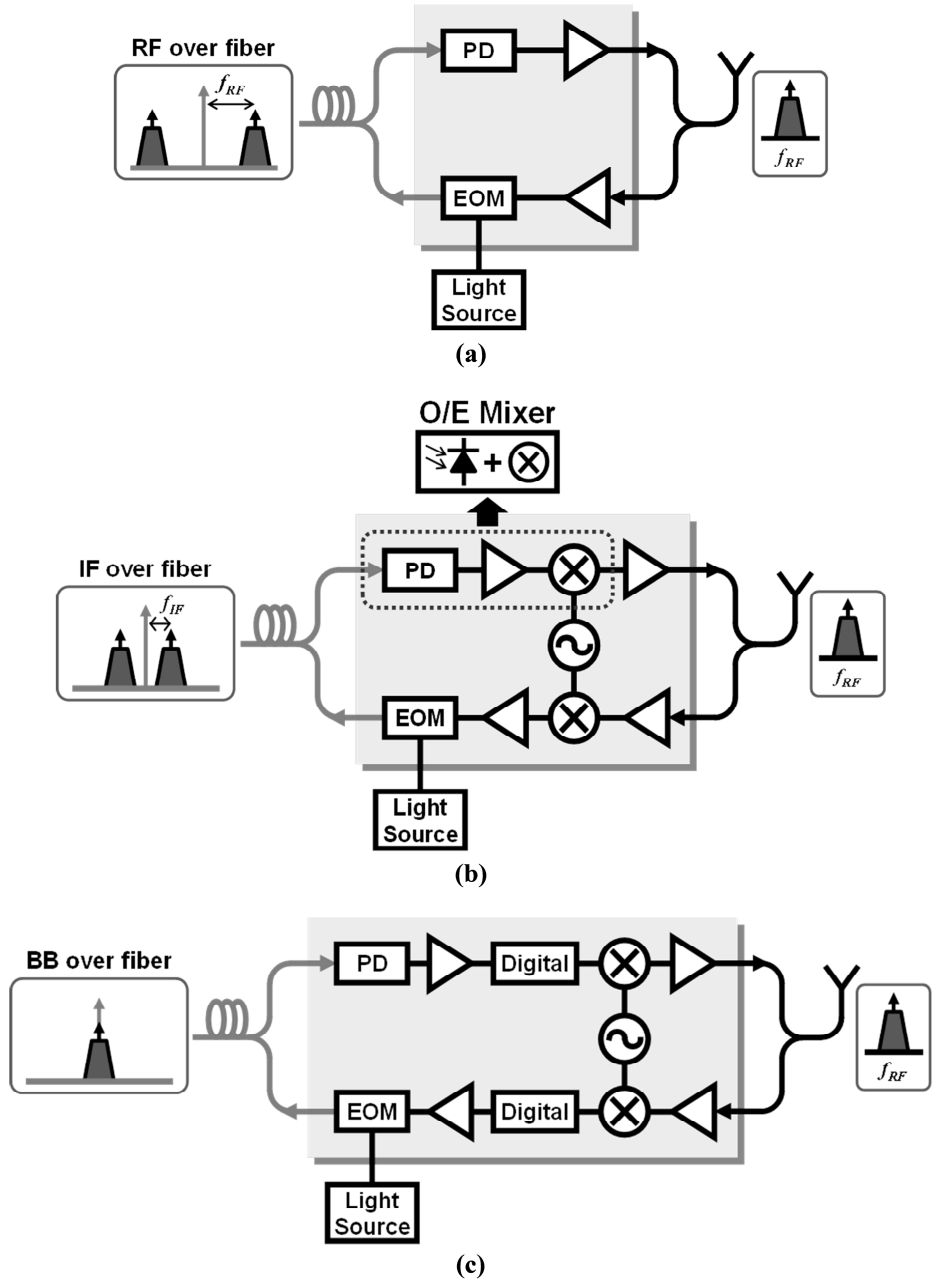

Fig. 1-2-1. Block diagrams of silicon integrated remote antenna units for (a) RF-over-fiber, (b) IF-over-fiber, and (c) baseband-over-fiber optical data distribution schemes.

Table 1-1
Comparison of fiber-wireless network architectures.

NETWORK ARCHITECTURE	RF OVER FIBER	IF OVER FIBER	BASEBAND OVER FIBER
Bandwidth of Photonic Devices (EOM and PD)	High*	Moderate	Low
Frequency Conversion	CO	Both	RAU
Wireless Network Control	CO	Both	RAU
CO Complexity	High	Moderate	Low
RAU Complexity	Low	Moderate (Simpler w/ O/E mixer)	High
Fiber Chromatic Dispersion	High	Moderate	Low

*Hard to support millimeter-wave band with silicon photonics technology

1-3. Photonics-Wireless Interface IC in Standard Silicon Technology

Even though silicon photonics is the most promising technology to develop silicon integrated RAUs, as of yet, there is no currently available silicon technologies generally supporting integrated germanium PDs and silicon EOMs with high-speed transistors in a single substrate. In an alternative approach, this dissertation focuses on standard CMOS/BiCMOS technologies since integrated silicon PDs can be realized with these technologies. Various types of CMOS-compatible PDs have been reported such as a lateral PIN PD [22], a spatially-modulated PD [23], and an avalanche PD (APD) [24] with the bandwidth of a few GHz. With those PDs, silicon integrated PWI ICs for downlink fiber-wireless network can be realized with standard CMOS/BiCMOS technologies. The PWI ICs using silicon PDs cannot operate at the 1550-nm wavelength inherently because of low absorption coefficient of silicon PDs at this wavelength. Nevertheless, this approach is a worthy initial attempt to investigate silicon RAUs because it can be easily extended into 1550-nm application when complete silicon photonics technology becomes available.

In this dissertation, three types of PWI ICs based on different RAU

structures are developed with silicon APDs [24] operating at the wavelength of 850 nm. For the RF-over-fiber structure, a PWI IC for 5-GHz WLAN application is implemented with standard CMOS technology. Secondly, as an IF-over-fiber PWI IC for millimeter-wave application, a 60-GHz balanced subharmonic O/E mixer (SHOEM) with standard BiCMOS technology is demonstrated. At last, for millimeter-wave baseband-over-fiber structure, a 60-GHz PWI IC with binary phase-shift keying (BPSK) modulation is developed with standard BiCMOS technology. Their performance and the feasibility are evaluated with fiber-wireless link demonstrations.

1-4. Outline of Dissertation

In chapter 2 describes the 5-GHz silicon PWI IC in standard CMOS process. In section 2-2, gain and noise analyses of the PWI IC using a 2-port network model are discussed. Section 2-3 describes the device description of the CMOS-compatible APD, its characterization, and its equivalent circuit model. Using the established APD model, implementation of the PWI IC is described in section 2-4. Circuit measurement results and 5-GHz WLAN data transmission results in fiber-wireless downlink are shown in section 2-5.

Chapter 3 describes two different approaches for the 60-GHz PWI ICs. One is the balanced SHOEM for IF-over-fiber RAU, and the other is the integrated baseband photoreceiver and millimeter-wave transmitter IC for baseband-over-fiber RAU. Section 3-2 describes the operation principle and the device optimization of the balanced SHOEM and narrowband data transmission results in 60-GHz fiber-wireless downlink. Section 3-3 and 3-4 describe circuit implementation and measurement of the integrated 60-GHz PWI IC and demonstration results of 1.6-Gb/s BPSK data transmission using the PWI IC.

Finally, this dissertation is summarized in chapter 4.

2. 5-GHz Silicon Photonics-Wireless Interface IC

2-1. Introduction

This chapter describes the 5-GHz silicon PWI IC for RF-over-fiber RAU fabricated with standard CMOS technology [25]. Fig. 2-1-1 shows the block diagram of the 5-GHz PWI IC consisting of an APD, a preamplifier, and a power amplifier (PA). Optically transmitted 5-GHz narrowband data with the RF-over-fiber scheme are converted into electrical data by the APD. And they are amplified by the preamplifier and the PA to radiate the data into the wireless channel with high power. The PWI IC is targeting 54-Mb/s 64 quadrature amplitude modulation (QAM) orthogonal frequency-division multiplexing (OFDM) 802.11 5-GHz WLAN application.

In order to enhance the optical input sensitivity, the PWI IC should be designed to have low noise. For this, noise characteristics of not only the preamplifier but also the APD should be analyzed since the overall noise performance of the PWI IC is affected by both of them. Power budget for wide dynamic range is determined as shown in Table 2-1. Assuming the maximum optical input power of 0 dBm and the PD responsivity of 0.1 A/W, the transimpedance gain of the PWI IC should

not exceed 80 dBΩ for the maximum available PA output power of 10 dBm. For this reason, the PWI IC is designed to have the gain of 80 dBΩ and the output 1-dB gain compression point of 13 dBm, including PA back-off.

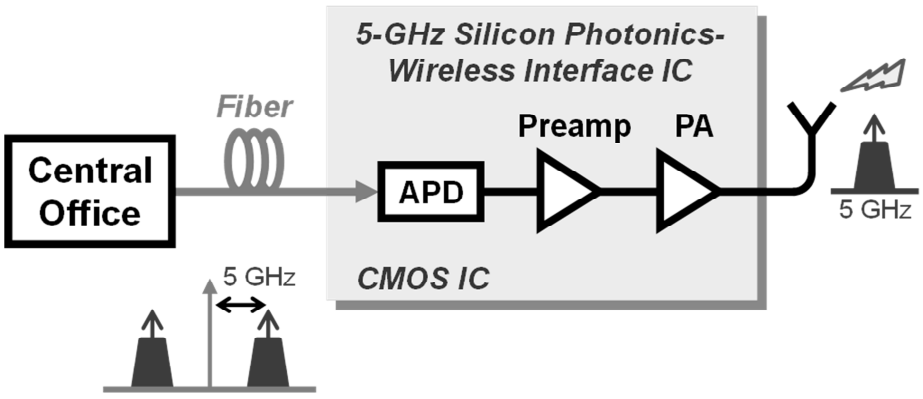

Fig. 2-1-1. Block diagram of 5-GHz PWI IC in standard CMOS technology for RF-over-fiber RAU.

Table 2-1
Power budget for 5-GHz PWI IC.

	GAIN	POWER
Optical Input Power	-	**0 dBm**
PD Responsivity	0.1 A/W	-
Photodetected Current	-	−80 dBA_{pk}
Transimpedance Gain (Preamp + PA)	**80 dBΩ**	-
Output Voltage	-	0 dBV_{pk}
Output Power w/ 50-Ω Load	-	**10 dBm**

2-2. Gain and Noise Analyses Using 2-Port Network Model

Fig. 2-2-1 shows a 2-port network model of the 5-GHz PWI IC. It is composed an APD, a matching network, and an amplifier. The APD block is an equivalent circuit model of the APD driven by the current sources i_{ph} and $i_{n,ph}$ representing the photocurrent and the shot noise induced by the photocurrent, respectively. The APD model should take into account the finite carrier transit time because the photodetection bandwidth is determined by not only the RC time constant but also the carrier transit time [26]. With this model, low-frequency approximation can be applied to the input sources, and consequently, i_{ph} and $i_{n,ph}$ can be regarded as frequency-independent. $i_{n,c}$ represents the input-referred noise current contributed by the APD parasitics and the circuit. The total noise current becomes

$$\overline{|i_{n,tot}|^2} = \overline{|i_{n,ph}|^2} + \overline{|i_{n,c}|^2} .$$

The matching network is placed between the APD and the amplifier to maximize the signal transfer and to minimize the circuit noise. The general expressions for the transimpedance gain and the equivalent input circuit noise current are well derived in [27], [28]. As a brief review, the transimpedance gain can be expressed by the equation

$$Z_T = \left| \frac{v_o}{i_{ph}} \right| = \frac{1}{2} \sqrt{G_{T,Amp} \frac{Z_0}{G_i}}$$

where $G_{T,Amp}$ is the transducer power gain of the amplifier for $\Gamma_L = 0$ given by [29]

$$G_{T,Amp} = \frac{1 - |\Gamma_S|^2}{|1 - S_{11}\Gamma_S|^2} |S_{21}|^2$$

$$= \frac{1 - |\Gamma_{MN}|^2}{|1 - S_{11}\Gamma_{MN}|^2} |S_{21}|^2$$

with the scattering parameters S_{ij} of the amplifier, and G_i is the intrinsic conductance given by

$$G_i = \mathrm{Re}\left\{ a_{21}^* a_{22} \right\}$$

with the chain matrix coefficients a_{ij} of the cascaded APD and matching network block. Because G_i is fixed for a given APD [27], maximizing Z_T is identical to maximizing $G_{T,Amp}$. The maximum Z_T is obtained when

$$\Gamma_{MN} = S_{11}^* .$$

The input-referred circuit noise current $i_{n,c}$ can be also found in [27], [28] as follow

$$\overline{|i_{n,c}|^2} = 4kT_0 df G_i F_{Amp}$$

where k, T_0, df, and F_{Amp} are Boltzmann constant, the reference temperature, the bandwidth, and the noise figure of the amplifier.

Similarly with the transimpedance, minimizing $i_{n,c}$ is identical to minimizing F_{Amp}. The equation for F_{Amp} is given by [29]

$$F_{Amp} = F_{\min,Amp} + \frac{R_{n,Amp}}{\mathrm{Re}\{Y_S\}}\left|Y_S - Y_{opt,Amp}\right|^2$$

$$= F_{\min,Amp} + \frac{R_{n,Amp}}{\mathrm{Re}\{Y_{MN}\}}\left|Y_{MN} - Y_{opt,Amp}\right|^2$$

where $F_{min,Amp}$, $R_{n,Amp}$, and $Y_{opt,Amp}$ are the minimum noise figure, the noise resistance, and the source admittance resulting in $F_{min,Amp}$, respectively. The minimum $i_{n,c}$ is allowed by the condition

$$\Gamma_{MN} = \Gamma_{opt,Amp}\,.$$

As a result, the narrowband PWI IC has very similar design strategy with a low-noise amplifier (LNA) with the source reflection coefficient Γ_{MN}, and therefore LNA design optimization techniques can be applied for designing the amplifier and the matching network.

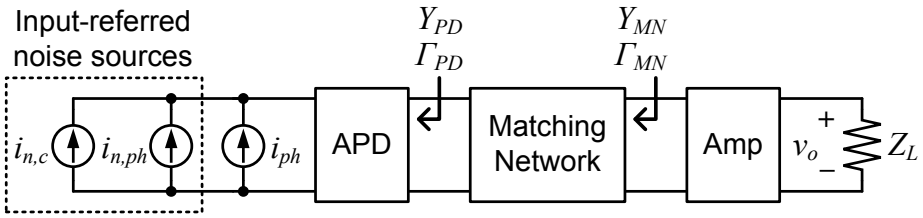

Fig. 2-2-1. 2-port network model of 5-GHz PWI IC.

2-3. APD in Standard CMOS Technology

2-3-1. Device Description

Fig. 2-3-1 depicts the cross-section view of an APD having an optical window of 10 μm × 10 μm available in standard CMOS technology without any design rule violation. In this structure, there exist two kinds of APDs formed at P^+/N-well junction and N-well/P-substrate junction, respectively. However, the N-well/P-substrate APD is hardly applicable due to lower avalanche gain and photodetection bandwidth than the P^+/N-well APD [30]. Isolating the N-well/P-substrate APD is available by collecting the output current at the P^+ port. And the reverse bias voltage is applied to the P^+/N-well APD by applying the positive voltage V_{PD} to the N-well port and 0 V to the P^+ port. By doing this, the electrons photogenerated by N-well/P-substrate APD cannot cross the reverse-biased P^+/N-well junction. Premature breakdown in the N-well/P-substrate junction does not happen because its breakdown voltage is much higher than P^+/N-well junction due to low doping concentration of P-substrate. Fig. 2-3-2 depicts the brief schematic of the 1-port APD configuration. 850-nm light from a laser diode is injected into the APD through a lensed fiber having 10-μm spot

diameter, which is same as the optical window of the APD. The P^+ port acts as a signal port and the N-well port is used only for biasing. An on-chip 8-pF decoupling capacitor explicitly provides AC ground path at the N-well port. Further details on the APD are given in [31].

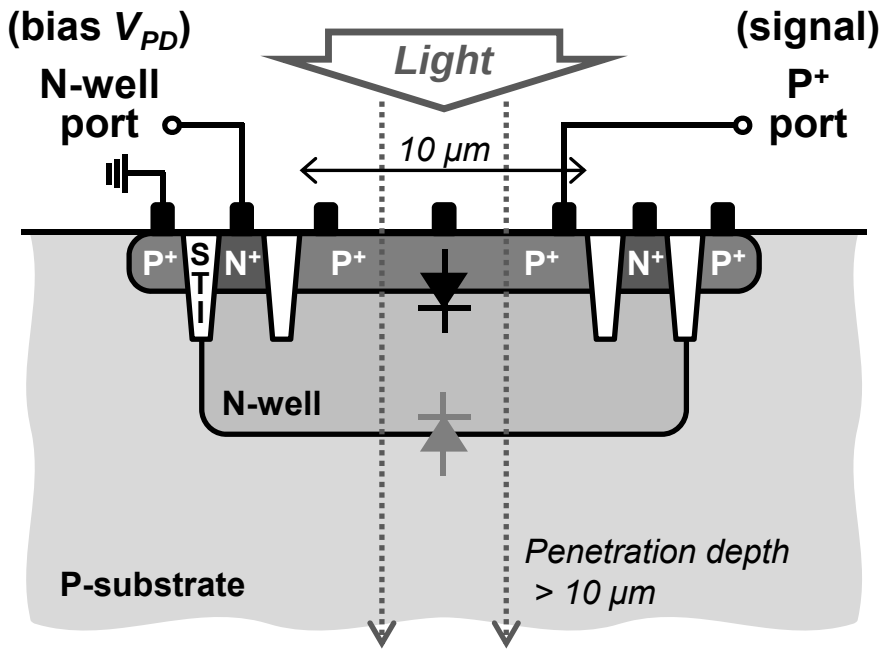

Fig. 2-3-1. Cross-section view of APD.

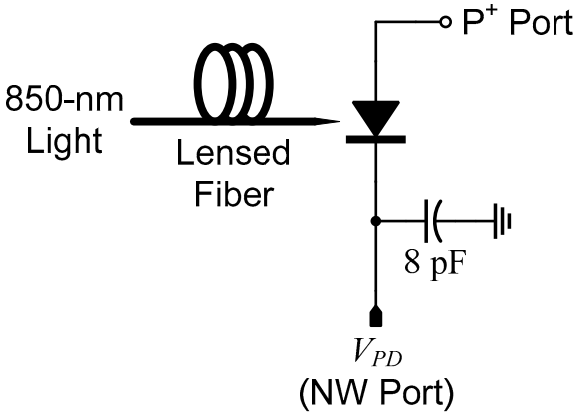

Fig. 2-3-2. Schematic of 1-port APD configuration.

2-3-2. DC and AC Characterization

DC characteristics of the APD under illumination and dark conditions are measured as shown in Fig. 2-3-3. For the illumination condition, the incident optical power is set to −8 dBm. Fig. 2-3-3 (a) shows the current-voltage characteristics of the APD. The dark current increases very sharply by avalanche multiplication process as the V_{PD} approaches the avalanche breakdown voltage of about 10.8 V. The photocurrent in the illumination condition also increases sharply but more gradually than the dark current. At V_{PD} higher than 10.8 V, both dark and photocurrents are saturated and become equal. DC responsivity and avalanche gain calculated from the current-voltage curves are shown in Fig. 2-3-3 (b). Responsivity and avalanche gain at 7.0 V have the values of only 0.018 A/W and 1.39. However, as V_{PD} increases they increase and have the maximum values of 7.09 A/W and 548.1 at 10.86 V.

The photodetection frequency responses at different V_{PD} are measured as shown in Fig. 2-3-4. For this measurement, a 20-GHz EOM is used to modulate the light from a laser diode and frequency responses from the modulator RF input to the APD output are measured by using a network analyzer. The measured response at higher bias

voltage has larger magnitude due to increased avalanche gain M. The 3-dB photodetection bandwidth is about 3.9 GHz in all cases.

The input impedance of the APD in the illumination condition at different V_{PD} is plotted on the impedance Smith chart as shown in Fig. 2-3-5. It is measured by a network analyzer and parasitics from probe pads and interconnection are calibrated out by using the pad-open-short deembedding technique [32]. The measured values are normalized by Z_0 of 500 Ω to observe their bias dependency more clearly. Open circles on the chart indicate the values at a frequency of interest, 5.4 GHz. Within the bias range from 9.2 V to 10.4 V there is nearly no difference in the input impedance while it becomes less resistive at higher V_{PD} due to abruptly increased avalanche gain.

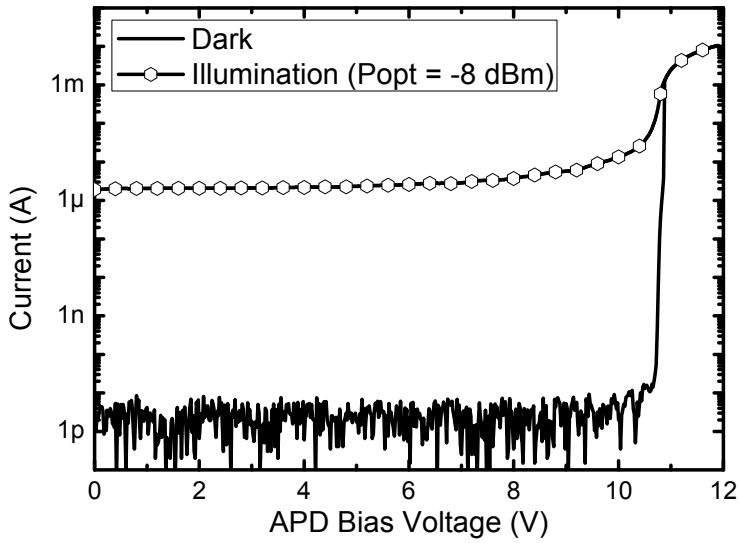

(a)

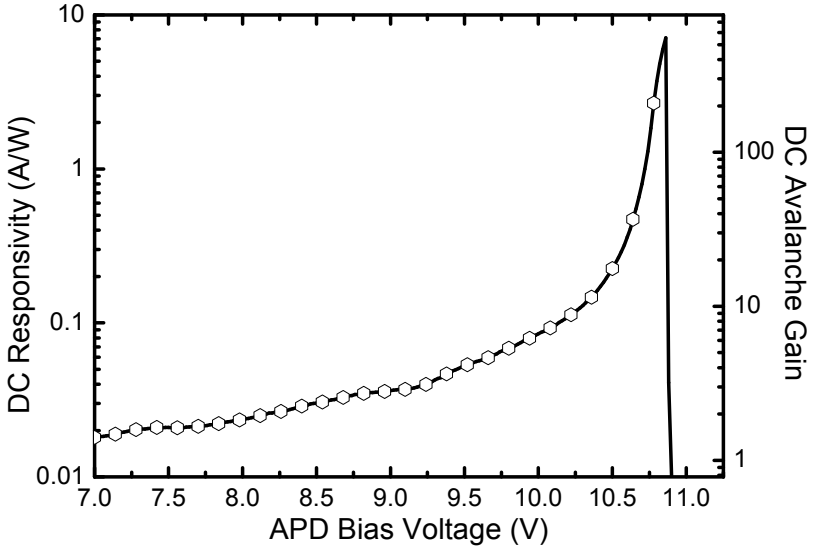

(b)

Fig. 2-3-3. (a) Current–voltage characteristics and (b) DC responsivity and avalanche gain of APD.

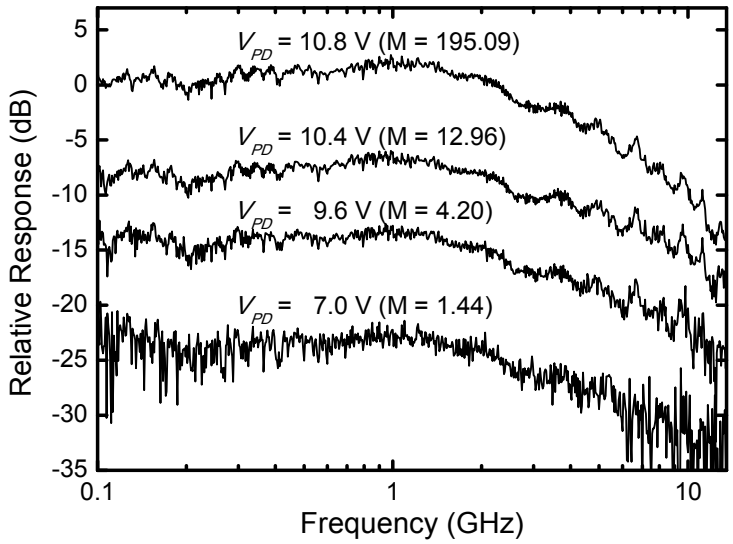

Fig. 2-3-4. Photodetection frequency responses of APD at different bias voltages.

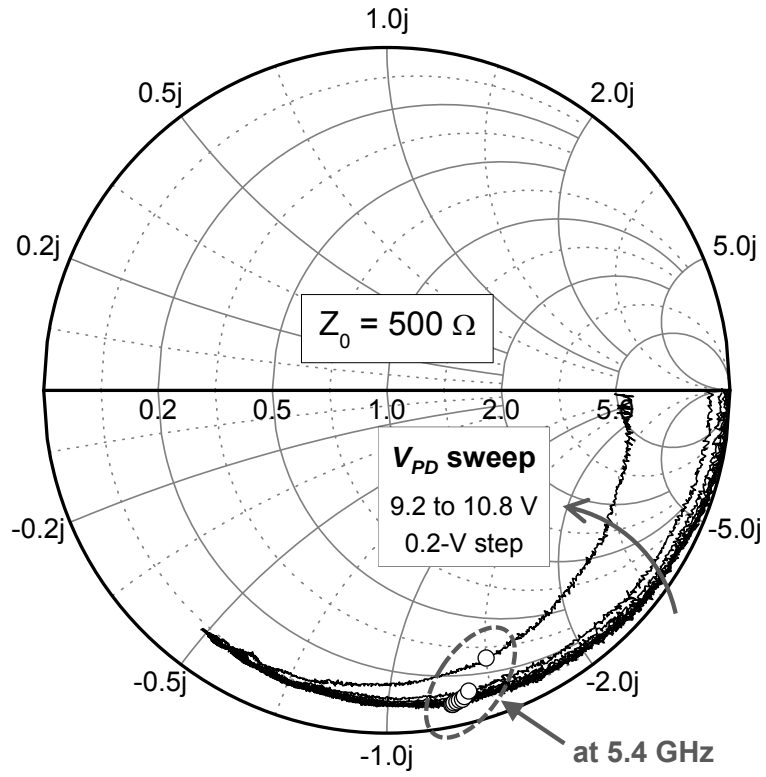

Fig. 2-3-5. Input impedance of APD on impedance Smith chart normalized by 500 Ω at different bias voltages. Open circles indicate input impedance at frequency of 5.4 GHz.

2-3-3. Noise Characterization

Even though the photogenerated signal current i_{ph} of the APD is directly proportional to the avalanche gain, the shot noise current $i_{n,ph}$ has higher rising slope due to excess noise during the multiplication process and is proportional to $M\sqrt{F}$ where F is the excess noise factor [33]. Therefore, investigating the noise performance of the APD depending on V_{PD} and determining its optimal bias condition for the best signal-to noise ratio (SNR) of the entire receiver is very important to design a following preamplifier. Fig. 2-3-6 depicts the experimental setup for signal and noise current measurements with WLAN data. Signal measurement is done by using the light modulated with 5.4-GHz −21-dBm WLAN data and noise measurement is done with the unmodulated light. In both measurements, power spectral densities of the APD output are measured by a spectrum analyzer. Two cascaded preamplifiers whose gain and noise figure are well characterized are placed between the APD and the spectrum analyzer to enhance measurement sensitivity. The measured power spectral densities are converted into the input-referred signal and noise current densities by carefully calibrating out added noise from preamplifiers, gain or loss of preamplifiers and cables, and frequency response of the APD.

Fig. 2-3-7 shows the input signal and noise currents of the APD, i_{ph} and $i_{n,ph}$ as a function of the avalanche gain, which is measured at DC as shown in Fig. 2-3-3 (b). The measured $i_{n,ph}$ at low avalanche gains involves the uncertainties in measurement caused by measurement sensitivity and calibration process. So it is fitted and extrapolated with assuming that it has the shot noise characteristic. The results indicate that i_{ph} increases with a slope of 1 and $i_{n,ph}$ increases with a slope of higher than 1. As a result, the SNR diminishes from 39.7 dB to 30.5 dB as the avalanche gain increases.

The SNR performance of the entire receiver is estimated from the measured $i_{n,ph}$ and three different $i_{n,c}$ cases. Fig. 2-3-8 (a) shows the input APD, circuit, and total noise currents while the circuit noise $i_{n,c}$ is set to 2, 5, and 10 pA/√Hz, respectively. The APD noise $i_{n,ph}$ increases rapidly as the bias approaches to the avalanche breakdown, while $i_{n,c}$ is constant in the entire bias region. As a result, $i_{n,tot}$ at the low bias region is affected by bias-independent $i_{n,c}$, but $i_{n,tot}$ at the high bias region is dominated by bias-dependent $i_{n,ph}$. Fig. 2-3-8 (b) shows how this affects the SNR performance. The SNR is obtained by calculating the ratio i_{ph} to $i_{n,tot}$. In case 1, the low circuit noise leads to the shot-noise characteristic in the almost entire bias range, so the SNR is gradually decreasing. In higher $i_{n,c}$ cases, on the other hand, the SNR is increasing

because the slope of the noise increment diminishes by the higher constant circuit noise and becomes less than the slope of the signal increment. At near-avalanche region, the three cases converge into the same SNR performance with very high $i_{n,ph}$. Since the input noise current of a preamplifier can be minimized to a few of pA/√Hz, a nominal SNR performance is expected to be case 2. With this assumption, the estimated operational V_{PD} range for the best SNR is from 9.0 V to 10.2 V.

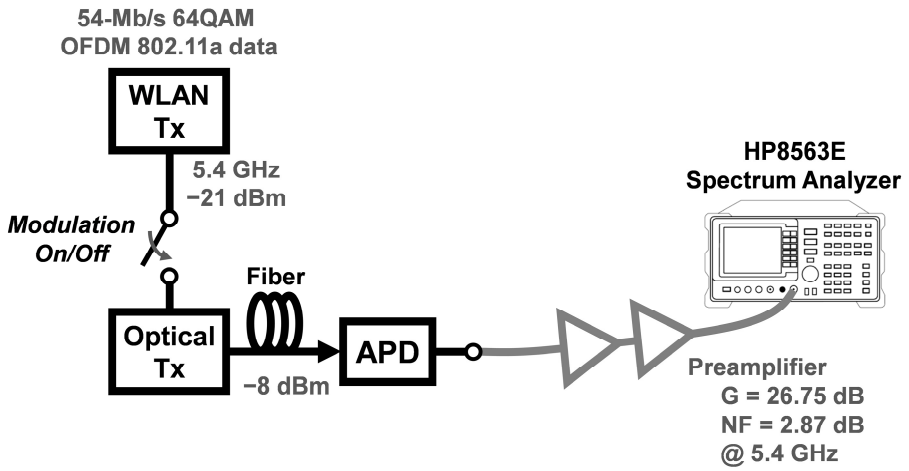

Fig. 2-3-6. Experimental setup to measure signal and noise currents of APD with WLAN data.

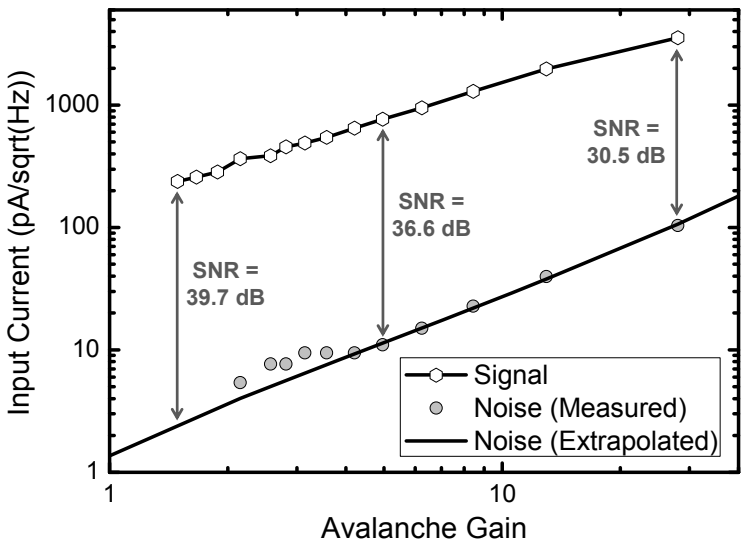

Fig. 2-3-7. Input signal and noise currents of APD as a function of avalanche gain.

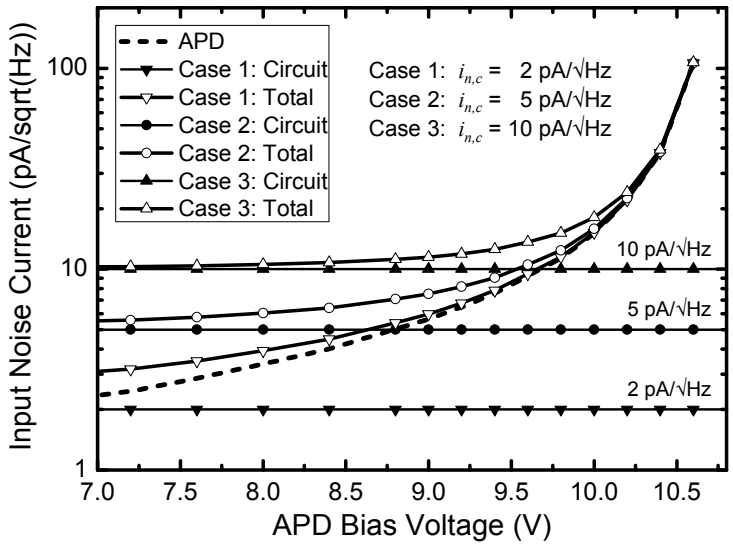

(a)

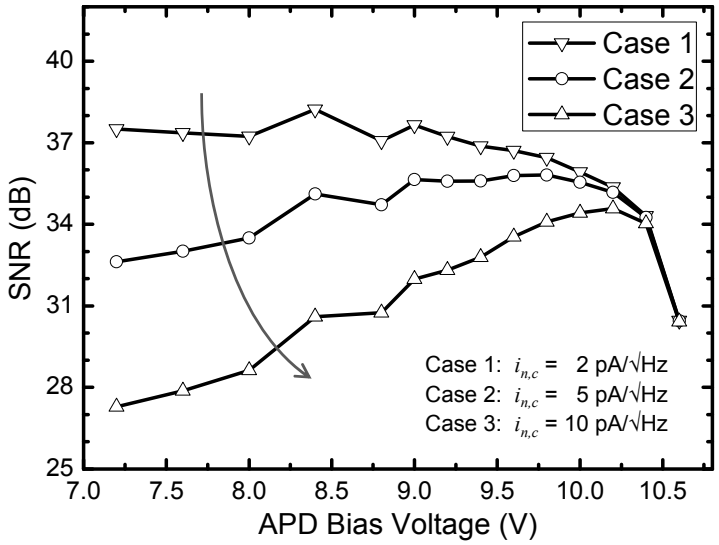

(b)

Fig. 2-3-8. (a) Input APD, circuit, and total noise currents and (b) total SNR as a function of APD bias voltage in different input circuit noise cases.

2-3-4. Small-Signal Equivalent Circuit Model

Fig. 2-3-9 illustrates the small-signal equivalent circuit model of the APD considering the transit time effect. R_j and C_j denote the junction resistance and capacitance of the P^+/N-well depletion region. R_s represents the N-well resistance from the P^+/N-well junction to the N-well electrodes. C_p is the parasitic capacitance between P^+ and N-well electrodes. The transit time effect is modeled with a current-controlled current source and a first-order RC lowpass filter (LPF) having its time constant equal to the transit time. Further descriptions on the model are given in [26]. One of the differences of our model from one in [26] is the absence of an inductive component representing the phase delay between current and voltage due to impact ionization. Within the operational V_{PD} range estimated in Section 2-3-3, this phase delay effect can be ignored because avalanche gain is not high enough yet. It can be verified by observing the input impedance as shown in Fig. 2-3-5. There cannot be observed any positive reactance points within the entire bias and frequency.

The model parameters are extracted from initial guess from theoretical equations and fitting to the measured characteristics at V_{PD} of 9.6 V, which is the median of the operational bias range. Because

there is nearly no difference in the input impedance within the operational V_{PD} range, the unified model can be established. The fitting process is as follows. At first, the passive parameters which are R_j, C_j, R_s, and C_p are extracted from the input impedance or admittance. Fig. 2-3-10 (a) shows the measured and fitted input impedance of the APD on the impedance Smith chart normalized by 500 Ω. And Fig. 2-3-10 (b) and (c) show the fitted results for real and imaginary part of the input admittance Y_{PD}, respectively. Secondly, the 3-dB bandwidth by transit time is extracted from the measured photodetection response. Fig. 2-3-11 shows the measured and fitted response with and without the transit time effect. The response of the model developed by electrical measurements without the transit time effect has much faster speed than the measured response. So it is fitted to the measured one by the LPF bandwidth f_{tr} representing the transit time effect. The extracted model parameters and the fitted values for the APD at V_{PD} of 9.6 V are listed in Table 2-2.

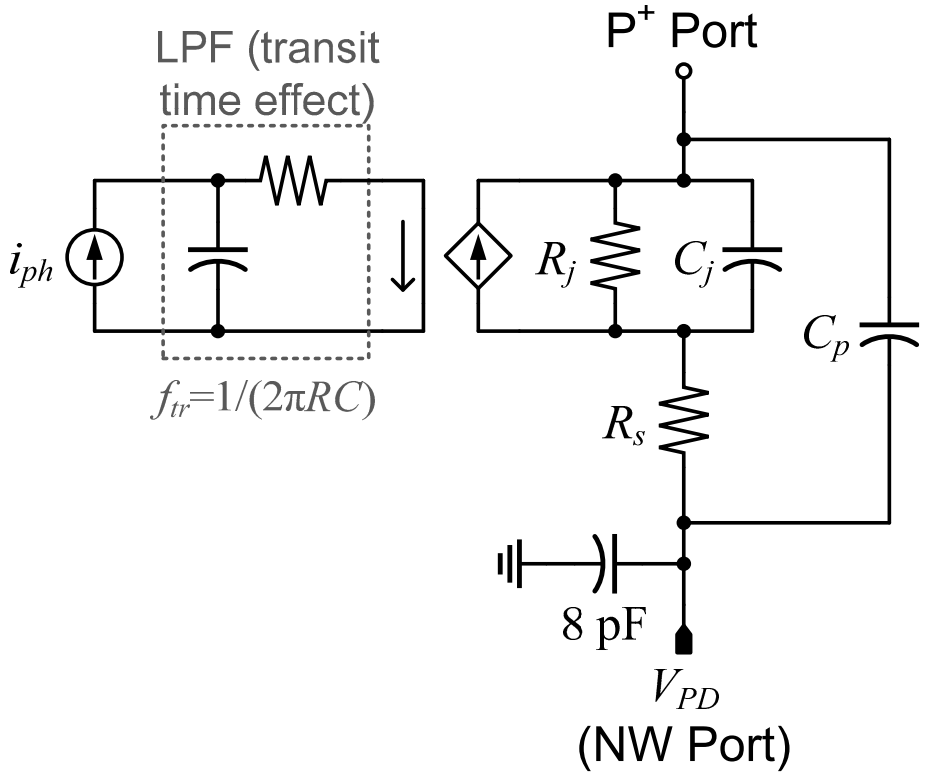

Fig. 2-3-9. Small-signal equivalent circuit model of APD considering transit time effect.

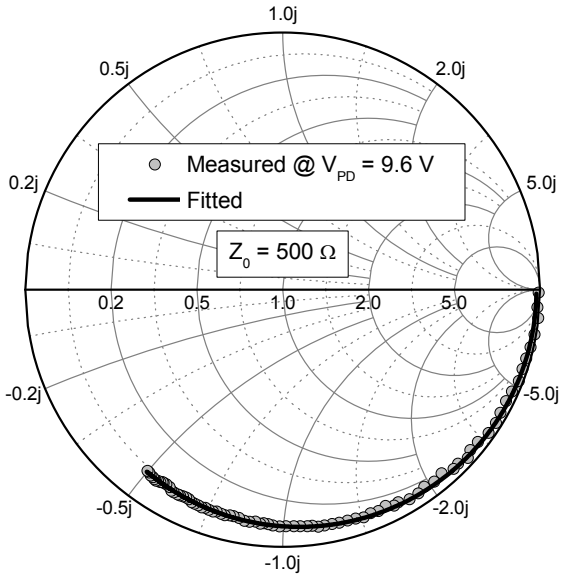

(a)

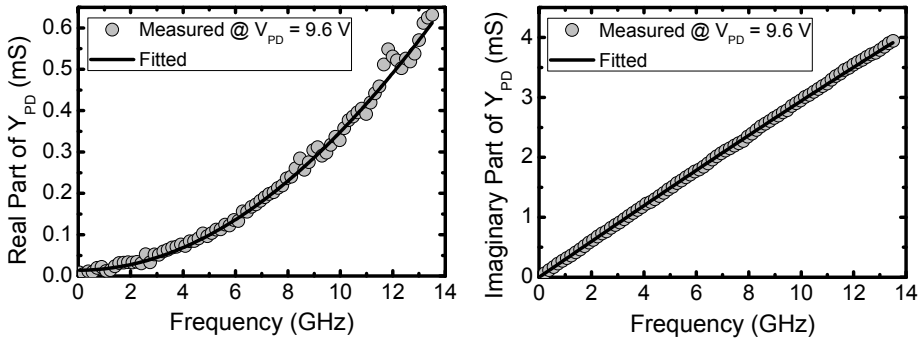

(b) **(c)**

Fig. 2-3-10. Fitted results of (a) input impedance of APD on impedance Smith chart normalized by 500 Ω and (b) real part and (c) imaginary part of input admittance at APD bias of 9.6 V.

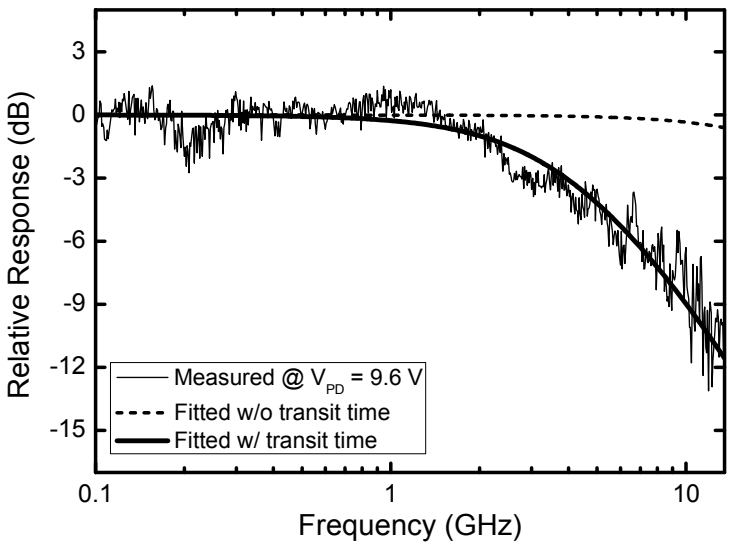

Fig. 2-3-11. Fitted results of photodetection frequency responses of APD with and without the transit time effect.

Table 2-2
Extracted model parameters and fitted values for APD at 9.6-V bias.

MODEL PARAMETERS	
Junction resistance, R_j	70 kΩ
Junction capacitance, C_j	35 fF
Series resistance, R_s	72 Ω
Parasitic capacitance, C_p	13 fF
Bandwidth from transit time, f_{tr}	3.98 GHz
FITTED VALUES	
Input admittance at 5.4 GHz, Y_{PD}	(0.113 + j1.608) mS
Photodetection bandwidth	3.92 GHz

2-4. Circuit Implementation

Fig. 2-4-1 shows the schematics of the 5-GHz PWI IC consisting of the APD, the preamplifier, and the PA. The bias circuits are not shown in this schematic. The design goal of the preamp is achieving low noise and high gain simultaneously. For this, a cascode LNA topology with the simultaneous noise and input matching technique [34] is used. The cascode configuration offers enough gain per stage to neglect the noise of the following amplifiers. The impedance matching between the preamp and the APD is carefully determined at 5.4 GHz with the equivalent circuit model of the APD. The matching is done by determining transistor size and current density of the preamplifier, a source degeneration inductor and a gate input capacitor of the preamplifier, and a shunt inductor, L_{shunt}. Especially, L_{shunt} is an essential component not only for the impedance matching but also for a DC current path for the APD. Even though a series inductor between the APD and the preamplifier makes the impedance matching more precisely, it is not considered in this design because it worsens the noise performance due to the parasitic resistance of a spiral inductor. The load of the preamplifier uses a parallel RLC topology with resonance at 5.4 GHz to have enough bandwidth. The PA is designed to supplement

gain and to drive an external 50-Ω load with large power handling capacity. The first stage uses a cascode topology for high gain, and the latter two stages utilize a common-source topology for high linearity. Each stage has a source-degeneration inductor to prevent unstable operation.

Fig. 2-4-2 shows the simulated transimpedance gain at the PA output v_o and the preamplifier output v_{o1} as a function of frequency. The peak gain of the preamplifier itself is 62.3 dBΩ at 5.4 GHz and the overall gain is 80.4 dBΩ after 18.1-dB amplification by the PA with a 50-Ω load. The 3-dB bandwidth is 0.6 GHz from 5.18 to 5.78 GHz. Fig. 2-4-3 shows the simulated total input noise current $i_{n,tot}$ at different input APD noise current $i_{n,ph}$. Simulations are performed with an additional noise source representing the measured $i_{n,ph}$ at each bias voltage, which are 5.63, 9.26, 21.99 pA/√Hz at 9.0, 9.6, and 10.2 V, respectively. The input-referred circuit noise current $i_{n,c}$ is minimized to 7.32 pA/√Hz at 5.35 GHz. The total noise currents with each APD noise are increased to 9.24, 11.8, and 23.2 pA/√Hz at the same frequency. Fig. 2-4-4 shows input-output power characteristics as a function of input signal current representing the photocurrent induced from the modulated optical signal. The output 1-dB gain compression point is about 13 dBm at the input signal current of −76 dBA or 158.5 μA. The gain compression is

occurred dominantly at the PA. Fig. 2-4-5 shows the return loss characteristic at the PA output. The return loss below −9.5 dB is obtained in the wide frequency range.

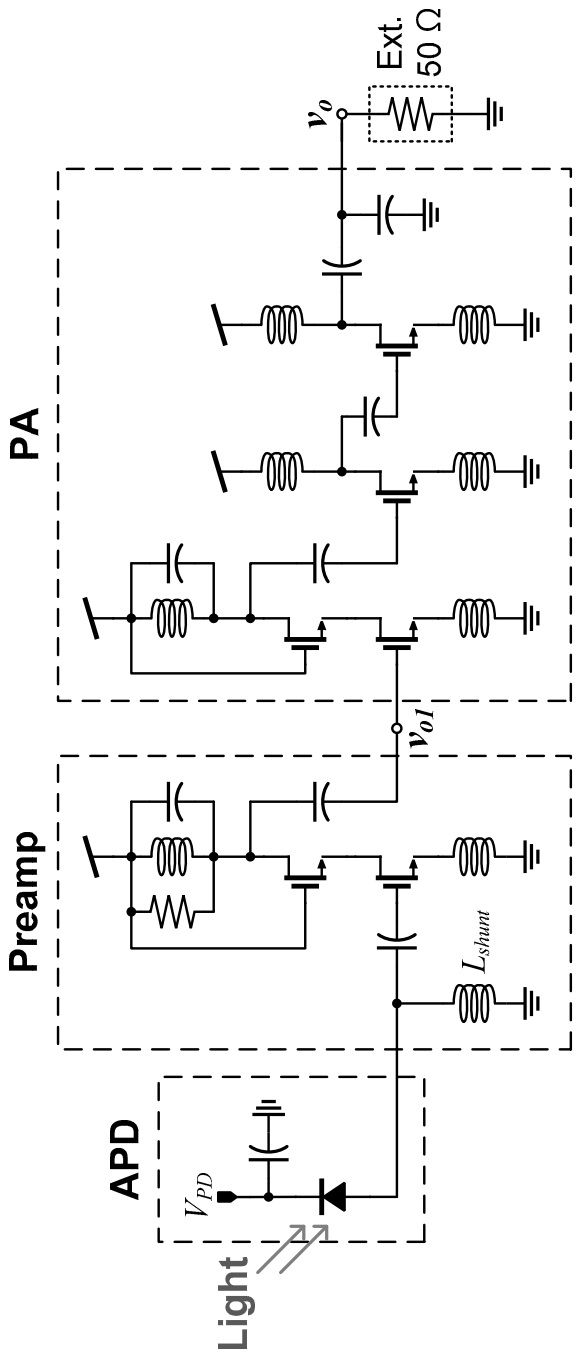

Fig. 2-4-1. Schematics of 5-GHz PWI IC in standard CMOS technology.

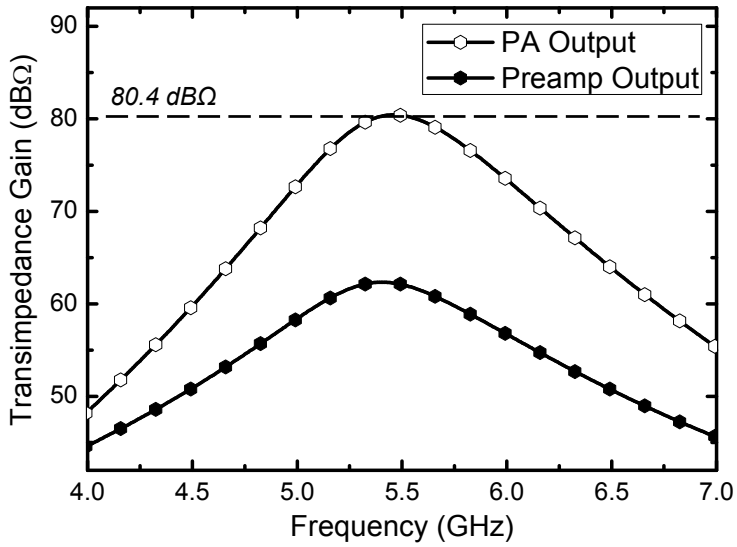

Fig. 2-4-2. Simulated transimpedance gain of 5-GHz PWI IC at PA output and preamplifier output as a function of frequency.

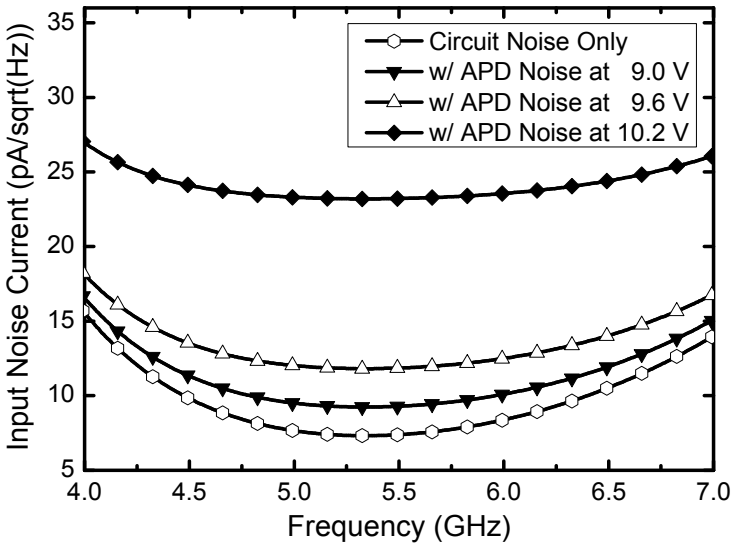

Fig. 2-4-3. Simulated input noise current at different input APD noise current as a function of frequency. APD noise currents at 9.0, 9.6, and 10.2 V are 5.63, 9.26, and 21.99 pA/√Hz, respectively.

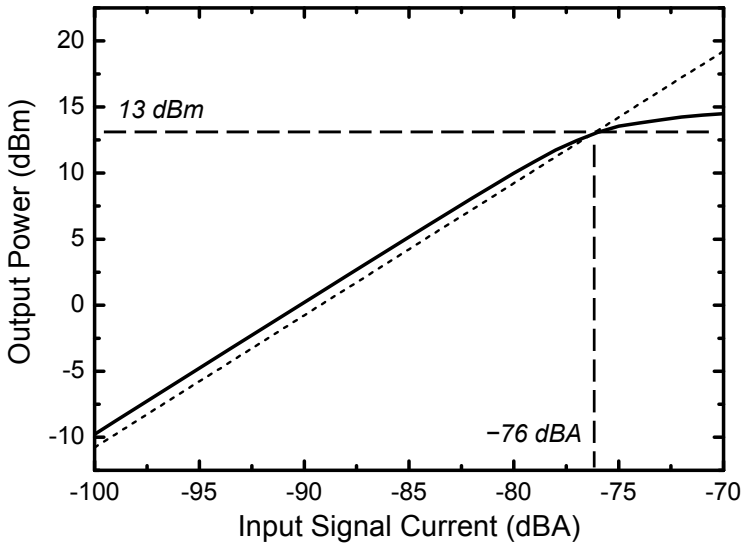

Fig. 2-4-4. Simulated output power of 5-GHz PWI IC as a function of input signal current.

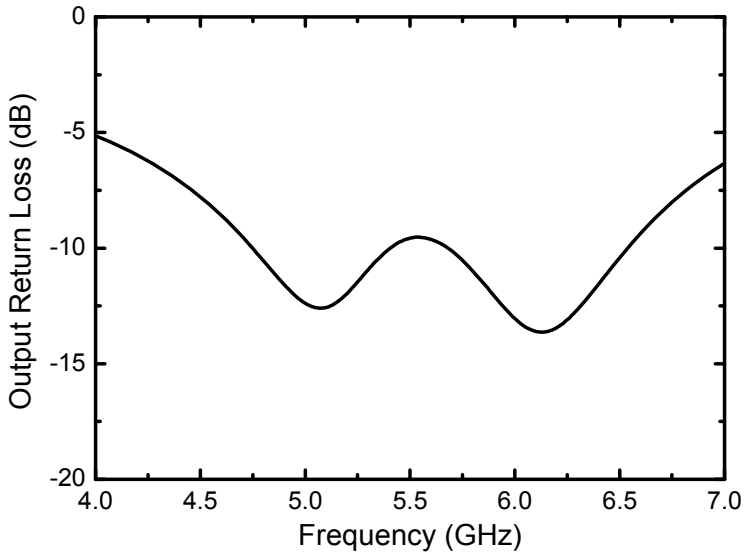

Fig. 2-4-5. Simulated output return loss of 5-GHz PWI IC as a function of frequency.

2-5. Experimental Results

2-5-1. Circuit Measurement

Fig. 2-5-1 shows the chip photo of the 5-GHz silicon PWI IC consisting of the APD, the preamplifier, and the PA. The APD bias V_{PD} and the RF output is connected to external measurement equipments through on-wafer probing setup with a DC probe pad and a RF ground-signal-ground pad, respectively. The spiral inductors are implemented with the 6-μm-width top metal except that the last stage of the PA uses the 15-μm-width inductors to handle high current. The chip area including all probe pads is 0.9 mm × 1.8 mm. The IC consumes power consumption is 155.7 mW from 1.8-V supply. The PA consumes most of the power due to its high-power driving performance.

The transimpedance gain Z_T is obtained indirectly by measuring two frequency responses of the APD and the entire PWI IC, respectively, as shown Fig. 2-5-2. Z_T as a function of frequency can be expressed by the equation

$$Z_T(f) = \left| \frac{v_o(f)}{i_{ph}} \right| = \frac{\sqrt{P_o(f) Z_0}}{\left| i_{ph} \right|}$$

where $P_o(f)$ is the output power at Z_0 load. Since i_{ph} is the low-frequency approximation of the output current of the APD, i_{ph} becomes

$$|i_{ph}| = |i_{APD}(f_{low})| = \sqrt{\frac{P_{APD}(f_{low})}{Z_0}}$$

where $i_{APD}(f)$, $P_{APD}(f)$, and f_{low} are the APD output current, the APD output power, and the low frequency near DC. Then Z_T can be rewritten as follows

$$Z_T(f) = Z_0\sqrt{\frac{P_o(f)}{P_{APD}(f_{low})}} = Z_0\sqrt{\frac{P_o(f)}{P_i(f)}\frac{P_i(f)}{P_{APD}(f_{low})}}$$

$$= Z_0\sqrt{\frac{|S_{21,PWI}(f)|^2}{|S_{21,APD}(f_{low})|^2}} = Z_0\frac{|S_{21,PWI}(f)|}{|S_{21,APD}(f_{low})|}$$

or

$$Z_{T,dB}(f) = 20\log_{10}(Z_0) + S_{21,PWI,dB}(f) - S_{21,APD,dB}(f_{low})$$

$$= 33.98 + S_{21,PWI,dB}(f) - S_{21,APD,dB}(f_{low})$$

where $P_i(f)$, $S_{21,APD}$, and $S_{21,PWI}$ are the input power available from the network analyzer to the optical transmitter and the forward transmission coefficients of the APD and the PWI IC. Fig. 2-5-3 (a) and (b) show the measured S_{21} of each at the APD bias of 9.6 V. From these S_{21} results, the transimpedance gain is obtained as shown in Fig. 2-5-3 (c). The simulated transimpedance gain is also plotted for comparison. The results show a good agreement between the simulated and

measured gain except that the measured data have slightly lower peak gain and lower peak-gain frequency than the simulated data. The measured peak gain is 79.9 dBΩ at 5.42 GHz. The 3-dB bandwidth is about 0.5 GHz from 5.2 to 5.7 GHz.

The input circuit noise $i_{n,c}$ is obtained by measuring the output noise power of the PWI IC. During this measurement, the APD is operated in the dark condition so as not to include the APD shot noise in the output noise. The noise measurement setup is identical to the setup for the APD noise measurement as shown in Fig. 2-3-6. Fig. 2-5-4 (a) shows the simulated and measured output noise power density at the APD bias of 9.6 V. At 5.4 GHz the measured noise power is 1 dB lower than the simulated one and it is believed that the fabricated amplifier has 1-dB lower gain characteristic than simulation at this frequency. For low output noise region the measured results show higher level than the simulated results. This is caused by a measurement inaccuracy due to the sensitivity limit of the noise measurement setup. The peak output noise power is about -130 dBm/Hz at 5.42 GHz. The input circuit noise current is obtained by dividing the output noise power by the measured transimpedance gain and the result is shown in Fig. 2-5-4 (b). The measured input noise current is well matched with the simulated one at frequencies of interest near 5.4 GHz. Discrepancies at other frequencies

are caused by the noise measurement inaccuracy mentioned earlier. The measured minimum noise current is about 7.3 pA/√Hz at 5.38 GHz.

Fig. 2-5-5 shows the calculated and measured output total noise power at 5.4 GHz at different APD bias voltages. In this measurement, the APD is operated in the illumination condition with the incident optical power of −8 dBm so as to include the APD shot noise in the output noise. The calculated output total noise power is obtained by using the input APD noise current shown in Fig. 2-3-7 and the measured input circuit noise current and transimpedance gain. A very good agreement between calculation and measurement is seen in both circuit-noise and APD-noise dominant bias regions. This agreement justifies the bias-independent unified APD circuit model and the input-referred APD and circuit noise model.

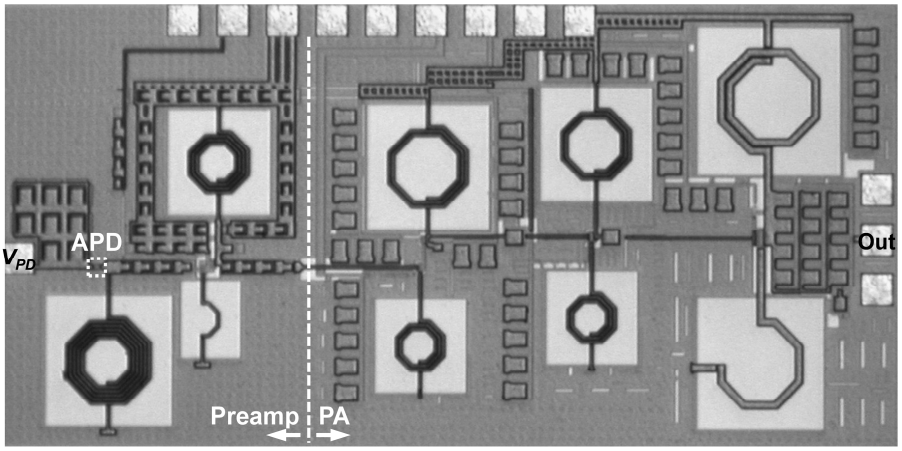

Fig. 2-5-1. Chip photo of 5-GHz PWI IC.

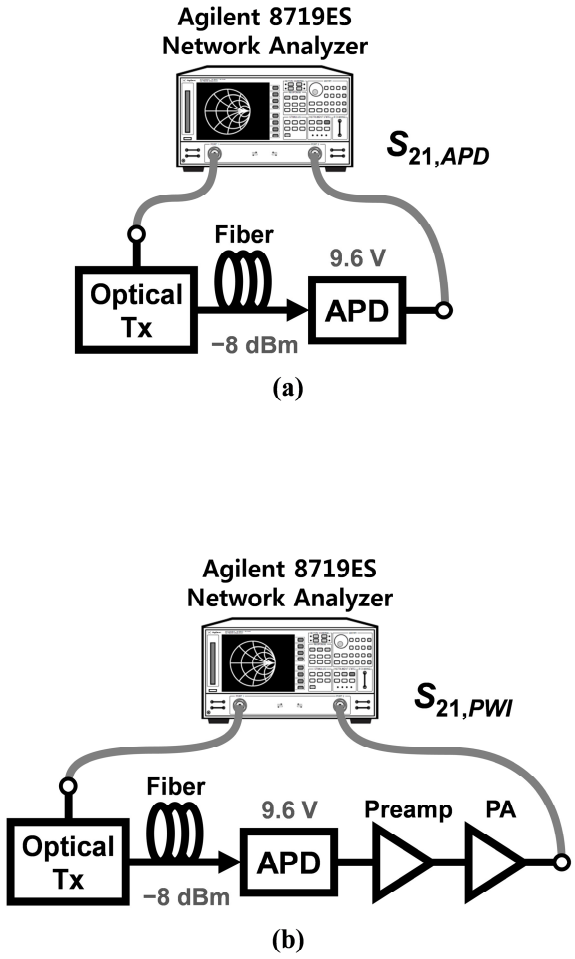

Fig. 2-5-2. Measurement setup for frequency responses of (a) APD and (b) entire 5-GHz PWI IC.

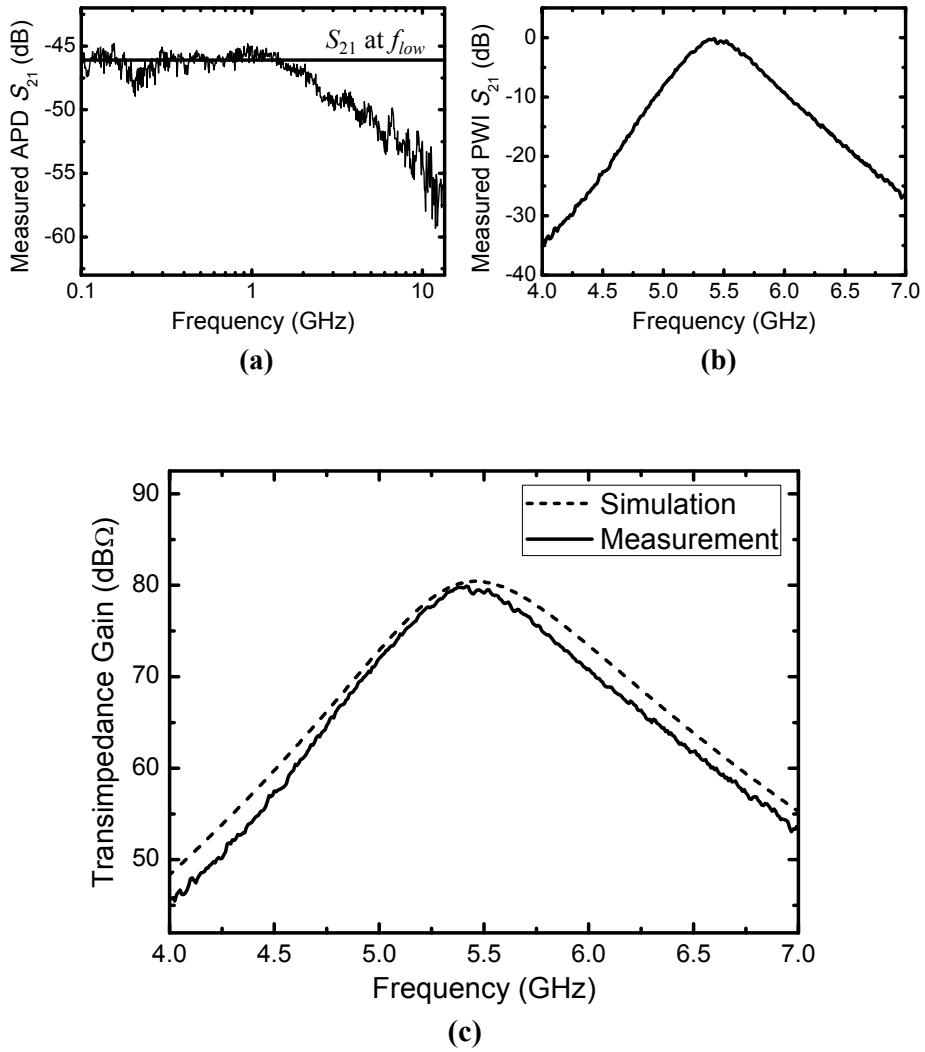

Fig. 2-5-3. Measured S_{21} of (a) APD and (b) 5-GHz PWI IC and (c) obtained measured transimpedance gain as a function of frequency. Simulated transimpedance gain is also plotted for comparison.

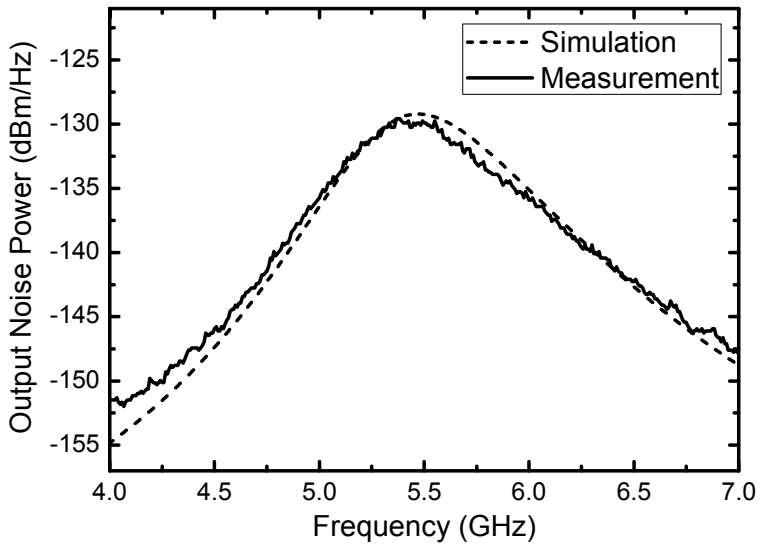

(a)

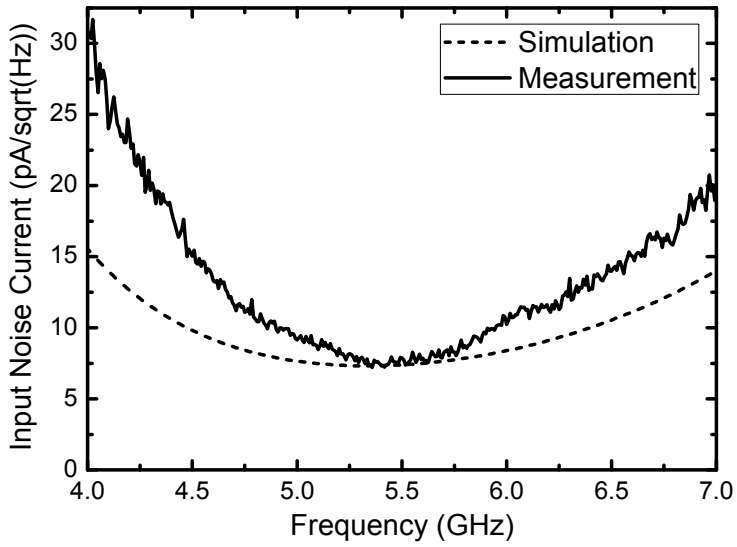

(b)

Fig. 2-5-4. Measured (a) output circuit noise power and (b) input circuit noise current of 5-GHz PWI IC as a function of frequency with APD biased at 9.6 V in dark condition. Simulated results are also plotted for comparison.

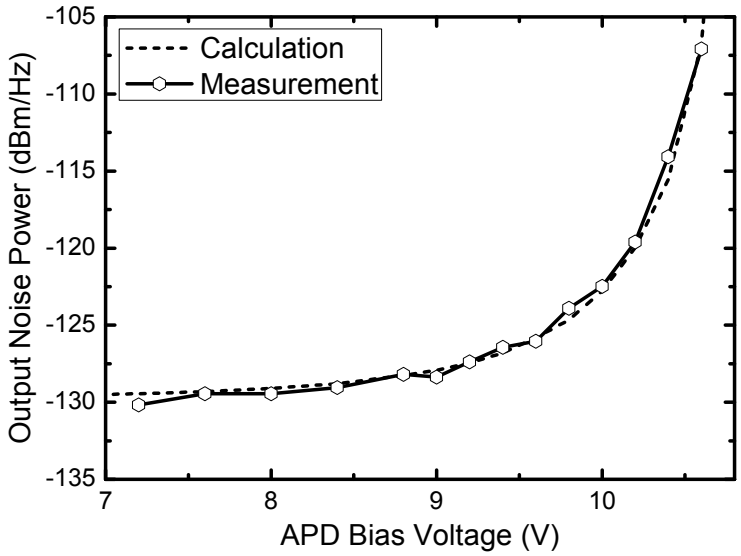

Fig. 2-5-5. Measured output total noise power of 5-GHz PWI IC at 5.4 GHz as a function of APD bias. Calculated results are also plotted for comparison.

2-5-2. Data Transmission

The fabricated PWI IC is demonstrated by data transmission of 54-Mb/s 64QAM OFDM 802.11 WLAN signals in 5-GHz fiber-wireless downlink. Fig. 2-5-6 depicts the demonstration setup. A WLAN transmitter which is a vector signal generator generates WLAN signals with the carrier frequency of 5.4 GHz. The optical transmitter consisting of an 850-nm laser diode and an EOM converts the WLAN signal from the WLAN transmitter into the optical signal. Input electrical power from the WLAN transmitter is set to −21 dBm because the signal with larger power is nonlinearized by the EOM. The optical signal is injected into the PWI IC through a 2-m-long multimode fiber and a lensed fiber. The PWI IC converts the optical signal into the wireless signal again, and the output signal is down-converted and its error vector magnitude (EVM) performance is evaluated by the WLAN receiver consisting of a mixer, a frequency synthesizer, an amplifier, and a vector signal analyzer.

Before measuring the EVM, the output power and the SNR of the PWI IC are obtained first. Fig. 2-5-7 (a) shows the measured output signal and noise powers at 5.4 GHz as a function of APD bias. The incident optical power is −8 dBm. The noise power data in this figure

are identical with Fig. 2-5-5. As the APD bias increases, the signal power also continuously increases due to increased avalanche gain. However, the increase of the noise power is slower than the signal power at the low APD bias region and faster at the high APD bias region. As a result, there exists APD bias region maximizing the SNR. Fig. 2-5-7 (b) shows the SNR performance at different APD bias. From the low bias, the SNR increases continuously until having the peak value of 35.5 dB at the APD bias between 9.6 V and 10.0 V. After that, the SNR declines rapidly due to the large APD shot noise.

Fig. 2-5-8 (a) shows the measured EVM at different APD bias voltages. The EVM is inversely proportional to the SNR shown in Fig. 2-5-7 (b), and the minimum EVM of 2.66% is obtained at 9.6-V APD bias. Fig. 2-5-8 (b) shows the EVM at different optical input powers. At low powers, the link performance degrades as optical input power decreases because the output signal power is reduced proportional to the optical input power but the noise power is not much reduced due to the circuit noise. Improvement in EVM and SNR with increasing optical IF power saturates from −8 dBm and it is believed that it is limited by the WLAN receiver. For 5.6% EVM, which is required in 64QAM modulation specified in IEEE 802.11 standardization [35], the optical input sensitivity is about −13 dBm. EVM degradation caused by

PWI IC nonlinearity is not seen because photodetection current is much lower than expected in the power budget shown in Table 2-1. This is caused by using small RF input power for EOM. Fig. 2-5-9 shows the measured power spectrum of the PWI IC output signal and demodulated data at the WLAN receiver at the optimum condition, which is the APD bias of 9.6 V and the optical input power of −8 dBm.

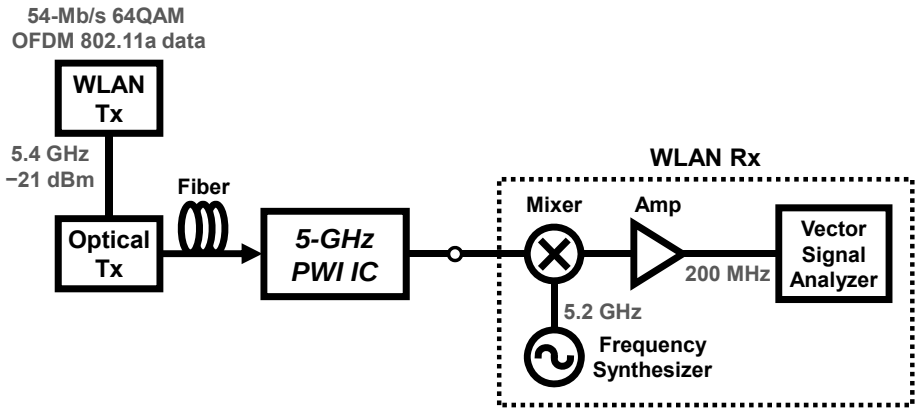

Fig. 2-5-6. Demonstration setup for 54-Mb/s 64QAM OFDM 802.11a WLAN data transmission in fiber-wireless downlink using 5-GHz PWI IC.

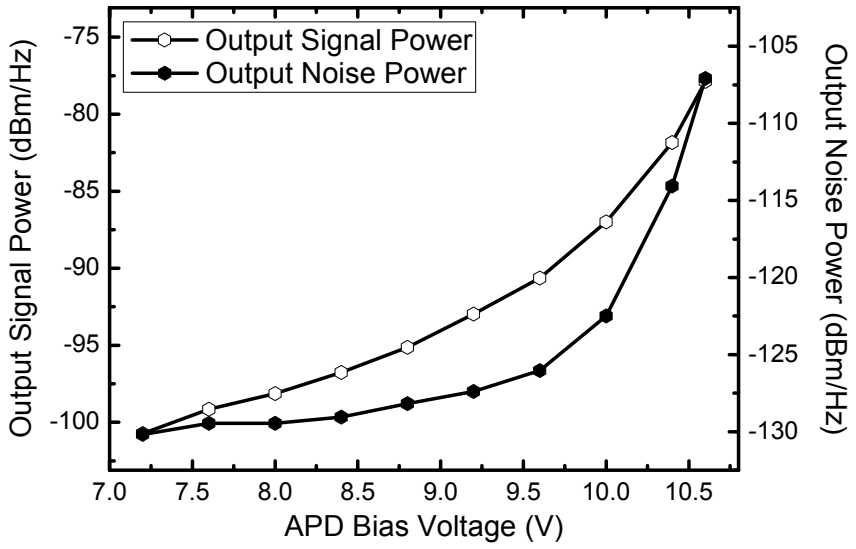

(a)

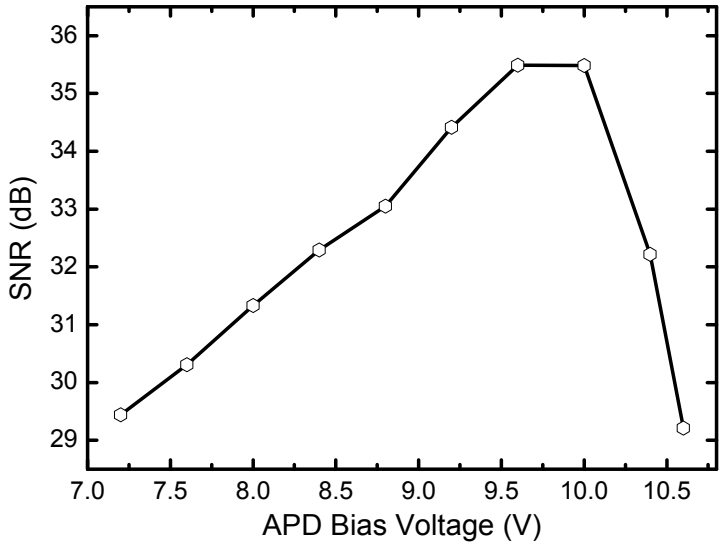

(b)

Fig. 2-5-7. Measured (a) output signal and noise power and (b) resulting SNR of 5-GHz PWI IC at 5.4 GHz as a function of APD bias. The incident optical power is −8 dBm.

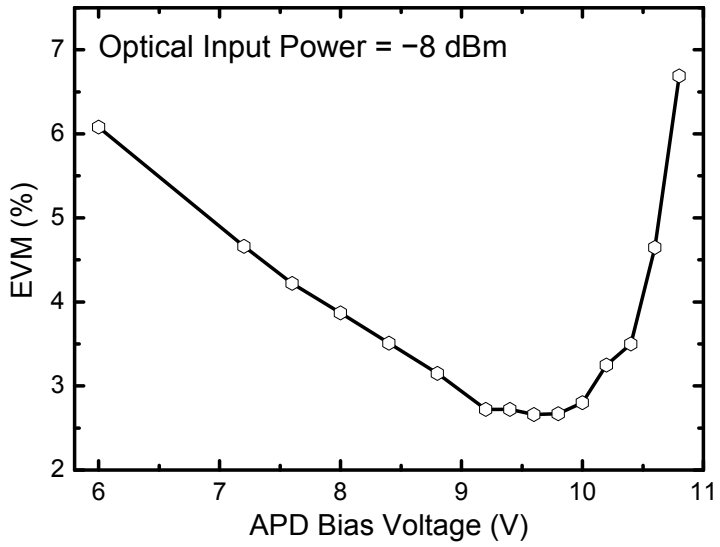

(a)

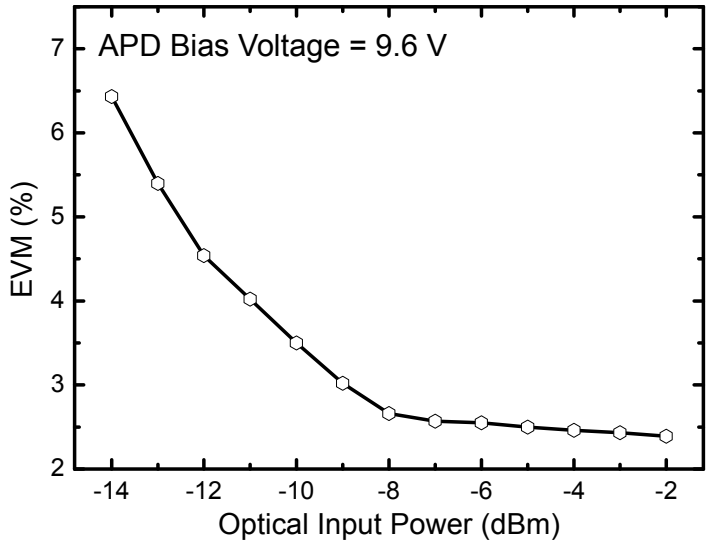

(b)

Fig. 2-5-8. Measured EVM performance of 5-GHz PWI IC at different (a) APD bias voltages and (b) optical input powers.

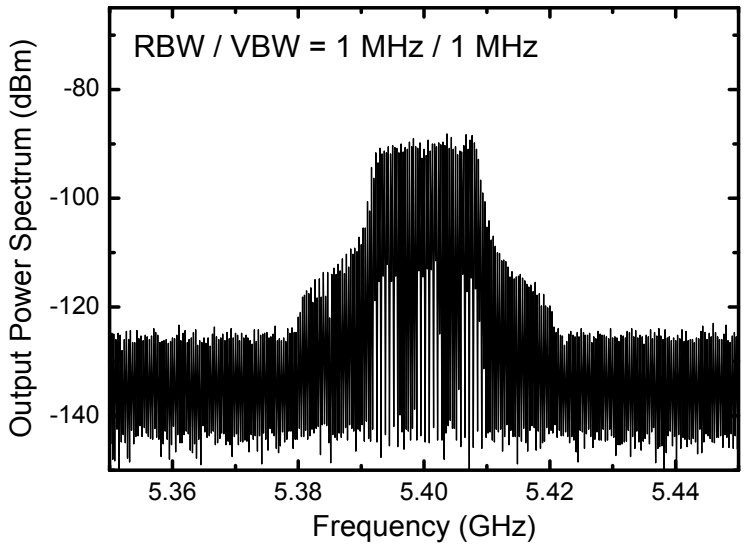

(a)

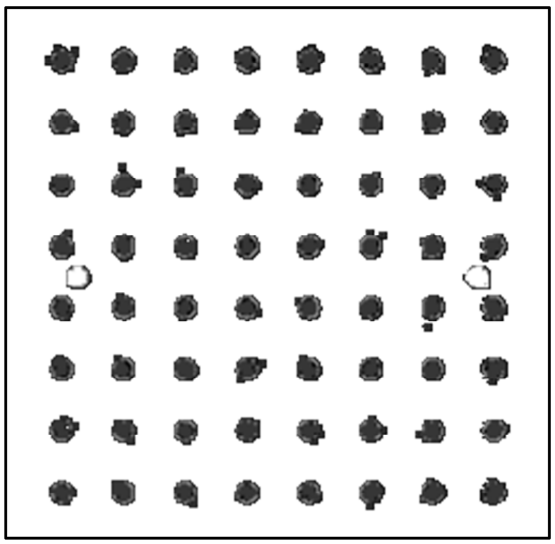

(b)

Fig. 2-5-9. Measured (a) output power spectrum of 5-GHz PWI IC and (b) constellation of demodulated data at WLAN Rx in the optimized condition; APD bias of 9.6 V and optical input power of −8 dBm.

2-6. Summary

The 5-GHz PWI IC in standard 180-nm CMOS technology is implemented with the accurately characterized on-chip APD. The experimental results including demonstration show its feasibility for realizing low-noise fiber-wireless link. Design and demonstration results of the PWI IC are summarized in Table 2-3.

Table 2-3
Performance summary of 5-GHz PWI IC.

DESIGN RESULTS	
Technology	180-nm RFCMOS
Photodetector	P^+/N-well APD (10 μm × 10 μm)
Frequency	5.4 GHz
Peak Transimpedance Gain	79.9 dBΩ at 5.42 GHz
Output 1-dB Comp. Point	13 dBm (simulation)
3-dB Bandwidth	0.5 GHz (from 5.2 to 5.7 GHz)
Minimum Input Circuit Noise	7.3 pA/√Hz at 5.38 GHz
Power Consumption	155.7 mW at 1.8-V supply
Chip Area	0.9 mm × 1.8 mm
DEMONSTRATION RESULTS	
Data Rate	54 Mb/s 64QAM
Optical Input Sensitivity	−13 dBm for 5.6% EVM
Optimum APD Bias Voltage	9.6 V
Minimum EVM	2.66% at −8-dBm optical power

3. 60-GHz Silicon Photonics-Wireless Interface IC

3-1. Introduction

As mentioned in chapter 1, 60-GHz PWI ICs were developed with two different approaches, which are the IF-over-fiber structure and the baseband-over-fiber structure. First, a 60-GHz silicon balanced SHOEM based on an APD pair in standard BiCMOS technology is developed for IF-over-fiber RAU [21], [36]. The APDs in BiCMOS technology are realized with CMOS process layers, so they are identical to APDs in CMOS process. The block diagram of the 60-GHz PWI utilizing the balanced SHOEM is shown in Fig. 3-1-1. IF-modulated optical data are converted into 60-GHz wireless data by the SHOEM. An external 30-GHz LO source is used for subharmonic mixing.

The second approach is a 60-GHz silicon PWI IC for baseband-over-fiber RAU which is integrated baseband photoreceiver and millimeter-wave transmitter as shown in Fig. 3-1-2 [37]. The integrated 60-GHz PWI IC consists of an APD, a transimpedance amplifier (TIA), a variable-gain amplifier (VGA), a BPSK modulator (BPSK MOD), and a PA. BPSK is chosen for wireless data modulation since it is one of the

modulation formats in 60-GHz standards [1], [2] and simplest to implement the modulator circuit.

This chapter is divided into two parts by the approaches. Section 3-2 describes the balanced SHOEM. And section 3-3 and 3-4 discusses circuit implementation and experimental results of the integrated 60-GHz PWI IC, respectively. Full descriptions of two approaches from device design to demonstration results are given in each part.

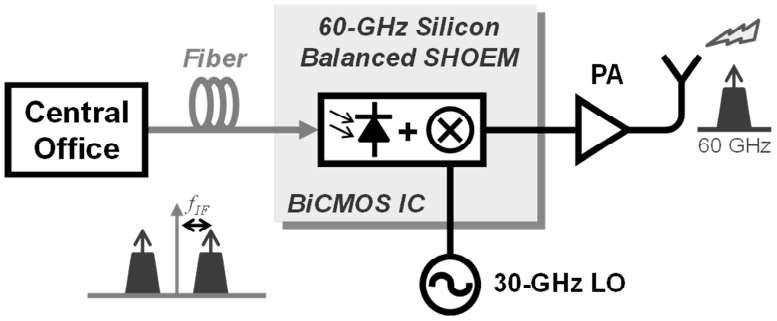

Fig. 3-1-1. Block diagram of 60-GHz PWI utilizing silicon balanced SHOEM in standard BiCMOS technology for IF-over-fiber RAU.

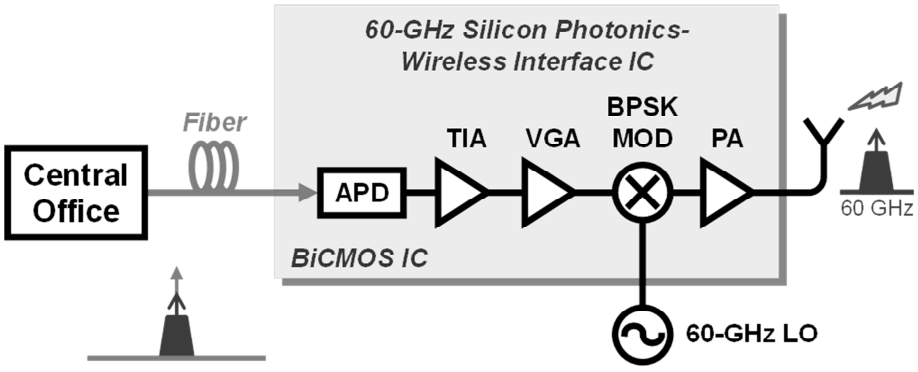

Fig. 3-1-2. Block diagram of integrated 60-GHz PWI IC in standard BiCMOS technology for baseband-over-fiber RAU.

3-2. Approach I – Balanced Subharmonic Optoelectronic Mixer Based on APD Pair

3-2-1. Operation Principle

This section reviews the operation principle of single and balanced SHOEMs based on APDs described in [36]. The SHOEMs use the nonlinear photodetection characteristic of the APD that the avalanche gain $M(V)$ is a function of the APD bias V_{PD} and increases abruptly as V_{PD} approaches the avalanche breakdown voltage. Fig. 3-2-1 shows the schematic and the operation principle of the single SHOEM. When the LO signal is applied to the APD biased at V_{PD} near breakdown, the avalanche gain is modulated by LO and, consequently, the photocurrent i_{ph} induced from the optical IF signal is frequency up-converted to the RF band. $i_{ph}(t)$ can be expressed by

$$\begin{aligned} i_{ph}(t) &= i_i(t)M(V_{PD} + v_{LO}(t)) \\ &= i_i(t)M_V(v_{LO}(t)) \end{aligned}$$

where $i_i(t)$ is the intrinsic IF photocurrent before avalanche multiplication process, $v_{LO}(t)$ is the LO voltage to be applied to the APD, and $M_V(v_{LO}(t))$ is the avalanche gain at the APD bias of V_{PD}.

Applying

$$i_i(t) = I_{IF} \cos \omega_{IF} t \,,$$

$$v_{LO}(t) = V_{LO} \cos \omega_{LO} t \,,$$

and the power series expansion for $M_V(v_{LO}(t))$

$$M_V(v_{LO}(t)) \approx m_0 + m_1 v_{LO}(t) + m_2 v_{LO}^2(t) + m_3 v_{LO}^3(t) \,,$$

$i_{ph}(t)$ can be rewritten as follow

$$i_{ph}(t) = \frac{I_{IF}(2m_0 + m_2 V_{LO}^2)}{2} \cos \omega_{IF} t + \frac{I_{IF}(4m_1 V_{LO} + 3m_3 V_{LO}^3)}{8} \cos(\omega_{LO} \pm \omega_{IF}) t$$
$$+ \frac{I_{IF} m_2 V_{LO}^2}{4} \cos(2\omega_{LO} \pm \omega_{IF}) t + \frac{I_{IF} m_3 V_{LO}^3}{8} \cos(3\omega_{LO} \pm \omega_{IF}) t$$

where I_{IF}, ω_{IF}, V_{LO}, and ω_{LO} are the amplitudes and the frequencies of the IF photocurrent and the LO voltage applied to the device, respectively. The desired conversion efficiency of the SHOEM is determined by the second-order nonlinear coefficient m_2 and V_{LO}. m_2 can be maximized by proper V_{PD}, but maximizing V_{LO} requires a large-size area-inefficient $\lambda_{LO}/4$ open stub to isolate LO and RF ports [38]. Without the port isolation, the most of supplied LO power passes to the RF port through the APD, and do not contribute to the frequency conversion. The APD junction capacitance also reduces V_{LO} because it lowers the junction impedance at high frequencies such as 30 GHz for this design and then larger LO power is consumed by the APD parasitic components such as the series resistance. The device shrink can be a

solution for smaller junction capacitance but limited by the spot diameter of a lensed fiber for injecting the optical signal.

The drawbacks of the single SHOEM can be solved by using the balanced SHOEM based on an APD pair [21]. The schematic and the operation principle of the balanced SHOEM are shown in Fig. 3-2-2. The structure of the APD pair is similar to singly balanced frequency doublers based on full-wave rectifying [39], [40]. Optical IF signals injected into two APDs generate in-phase photocurrent. The optical window area of each APD has half size of the APD using the single SHOEM in order that the total optical window of the balanced SHOEM is identical to the single SHOEM. When LO signals are differentially applied to the APD anodes, they modulate avalanche gain of two APDs in the opposite direction. Since the APD pair acts as a full-wave rectifier for the LO signals, a train of half-sinusoidal pulses consisting of even harmonics are produced, among which the second harmonic is dominant. Therefore, the resulting photocurrent i_{ph} at the RF port given by

$$\begin{aligned} i_{ph}(t) &= i_{ph+}(t) + i_{ph-}(t) \\ &= \frac{1}{2} i_i(t) M_V(v_{LO}(t)) + \frac{1}{2} i_i(t) M_V(-v_{LO}(t)) \\ &= \frac{I_{IF}(2m_0 + m_2 V_{LO}^2)}{2} \cos \omega_{IF} t + \frac{I_{IF} m_2 V_{LO}^2}{4} \cos(2\omega_{LO} \pm \omega_{IF})t \end{aligned}$$

has the frequency up-conversion component only at $2\omega_{LO} \pm \omega_{IF}$.

Because all the odd LO harmonics including the fundamental are rejected inherently, it requires no filtering of unwanted harmonics. Moreover, because the common node for two APDs acts as a virtual ground for LO, the inherent port isolation can be performed without the open stub as an advantage for smaller chip area. Also, the half-size APD has the smaller junction capacitance and is much effective to enhance the mixing efficiency while the responsivity is not much reduced because the total size is identical to the single SHOEM.

Performance of the single and balanced SHOEMs is compared with the total optical window of 10 μm × 10 μm. The SHOEMs are realized with CMOS process layers in IHP's 250-nm SiGe:C BiCMOS technology [41]. Fig. 3-2-3 shows measured 60.1-GHz up-converted RF signal powers of two SHOEMs at different APD bias voltages and 30-GHz LO powers, respectively. 0-dBm 100-MHz optical IF signal is used for these measurements. The balanced SHOEM has 11-dB conversion efficiency improvement over the wide range of bias voltages and LO powers.

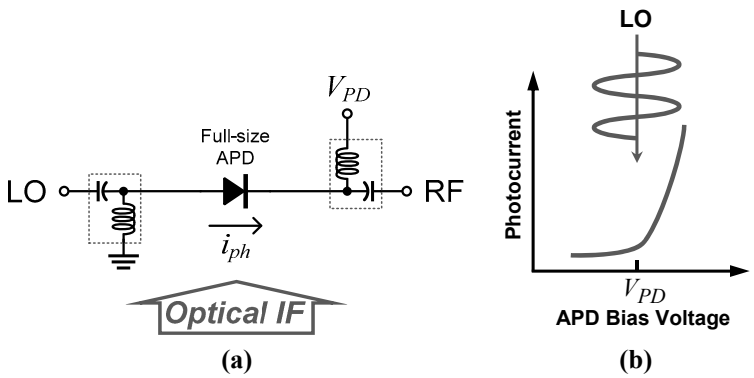

Fig. 3-2-1. (a) Schematic and (b) operation principle of single SHOEM.

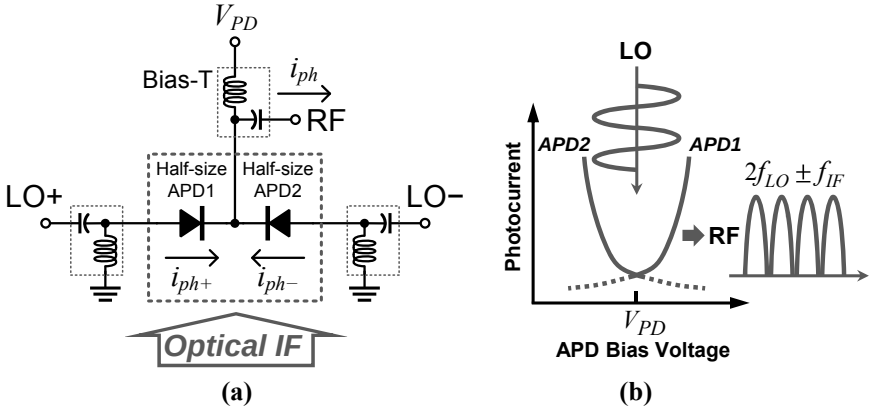

Fig. 3-2-2. (a) Schematic and (b) operation principle of balanced SHOEM.

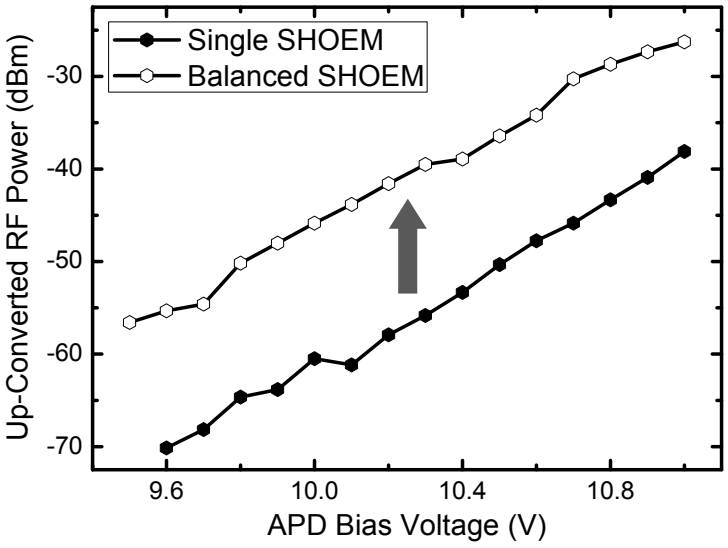

(a)

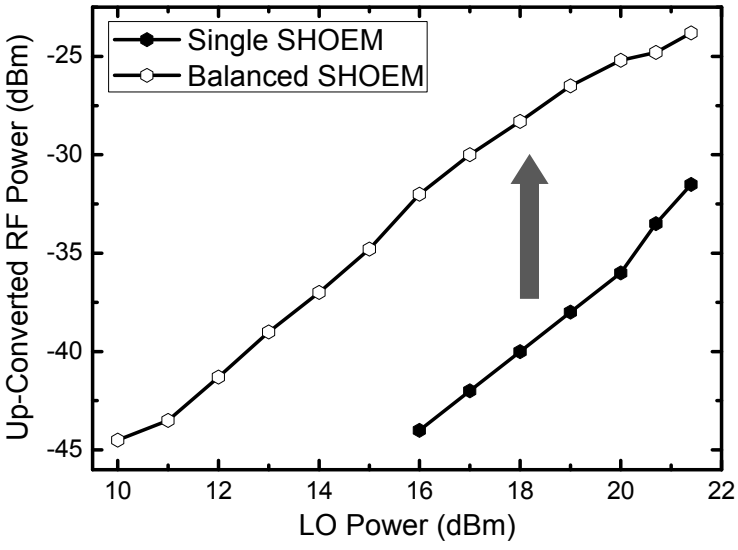

(b)

Fig. 3-2-3. Measured 60.1-GHz up-converted RF signal powers of single and balanced SHOEMs at (a) different APD bias voltages with 19-dBm LO power and (b) different LO powers with 11.0-V APD bias voltage.

3-2-2. Comparison of Common-N and Common-P Pairs

For the balanced SHOEM, two configurations for APD pairs are possible: common-N and common-P depending on the APD common RF output terminal as shown in Fig. 3-2-4. In the common-N type, LO signals are injected into the anodes of the pair, and RF output signals are collected from the common cathode as shown in Fig. 3-2-4 (a). In the common-P type, APDs are configured in the opposite direction as shown in Fig. 3-2-4 (b) so that RF signals are collected from the common anode.

DC, AC, and 60-GHz up-conversion characteristics of two types of balanced SHOEMs fabricated with 250-nm BiCMOS technology are compared to figure out the optimized structure. Fig. 3-2-5 (a) and (b) show the top-view layout and schematic cross-section of the common-N type. A pair of vertical PN junctions is formed by two separated P^+ regions and common N-well region. Each junction has the lateral dimension of 4 μm × 10 μm separated by 2 μm. The optical signal is vertically injected into two APDs through a lensed fiber having a spot diameter of 10 μm. The photocurrent is extracted from common N-well and collected into the RF output terminal. Differential LO signals are applied to P^+ regions. The top-view layout and schematic cross-section

for the common-P type are shown in Fig. 3-2-5 (c) and (d). Two separated N-well regions form independent cathodes for differential LO input signals. They are separated by 6 μm so that they are not affected by dopant diffusion. Each junction has the lateral dimension of 4 μm × 14 μm. The optical window size is little larger than the common-N type due to the separation between the N-well regions. RF output is collected from P^+ region in each N-well.

Fig. 3-2-6 shows current-voltage characteristics of two types under illumination and dark conditions. For illumination, the incident optical power of 0 dBm is injected into the devices. Avalanche breakdown voltages of two types have the same value of 11.2 V. The common-N type has much higher currents than the common-P type before avalanche breakdown. This is because both P^+/N-well junction and N-well/P-substrate junction contribute to output currents. N-well/P-substrate junction generates larger drift and diffusion currents than P^+/N-well junction because of lower doping concentration and larger charge neutral region [30]. The difference in currents decreases as avalanche currents in P^+/N-well junctions become larger near avalanche breakdown.

Fig. 3-2-7 shows relative photodetection frequency response of two types at the 11.0-V APD bias. The common-N type has 5.1-dB higher

response at low frequencies, but the common-P type has 1.7 times wider 3-dB bandwidth. Discrepancies of two responses can be explained by two factors: frequency-independent decrease of 2.7 dB in the common-P type and frequency-dependent increase of 2.4 dB at low frequencies in the common-N type. The frequency-independent decrease in the common-P type is caused by inefficient optical coupling. As shown in Fig. 3-2-5, the common-P type requires more spacing to separate two APDs than the common-N type, and therefore the common-P type absorbs less light than the common-N type, resulting in frequency-independent loss in the photodetection response.

The frequency-dependent increase in the common-N type originates from N-well/P-substrate junction effect. As mentioned earlier, N-well/P-substrate junction increases total photocurrents of the common-N type, so it increases the photodetection response at low frequencies. However, because carriers generated in this junction reach the output terminal by slow diffusion process [30], the increase vanishes at high frequencies, resulting in a decrease in the 3-dB bandwidth from 2.18 GHz to 1.25 GHz.

Fig. 3-2-8 shows 60.1-GHz up-converted RF signal powers of two types at different APD bias voltages. 100-MHz optical IF signals and 18-dBm 30-GHz LO signals are used for up-conversion measurements.

The up-converted power increases as the APD bias voltage increases, and it maximizes at 11.0 V. And the common-N type has 4 dB higher up-conversion efficiency than the common-P type.

As a result, the common-N type shows better up-conversion performance and the common-P type shows wider 3-dB IF bandwidth performance. This observation will be very useful for selecting the optimal device structure of silicon APD pairs for given applications.

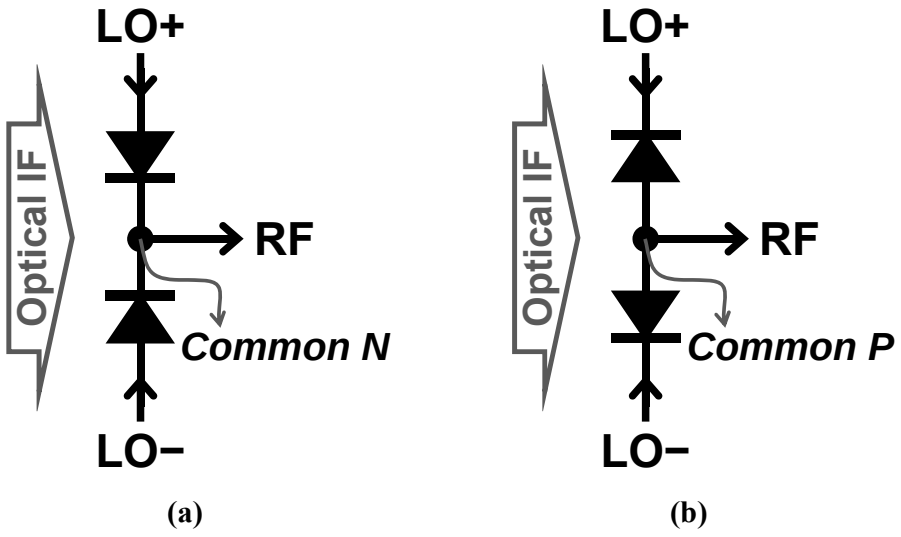

Fig. 3-2-4. Device configuration of (a) common-N and (b) common-P balanced SHOEMs.

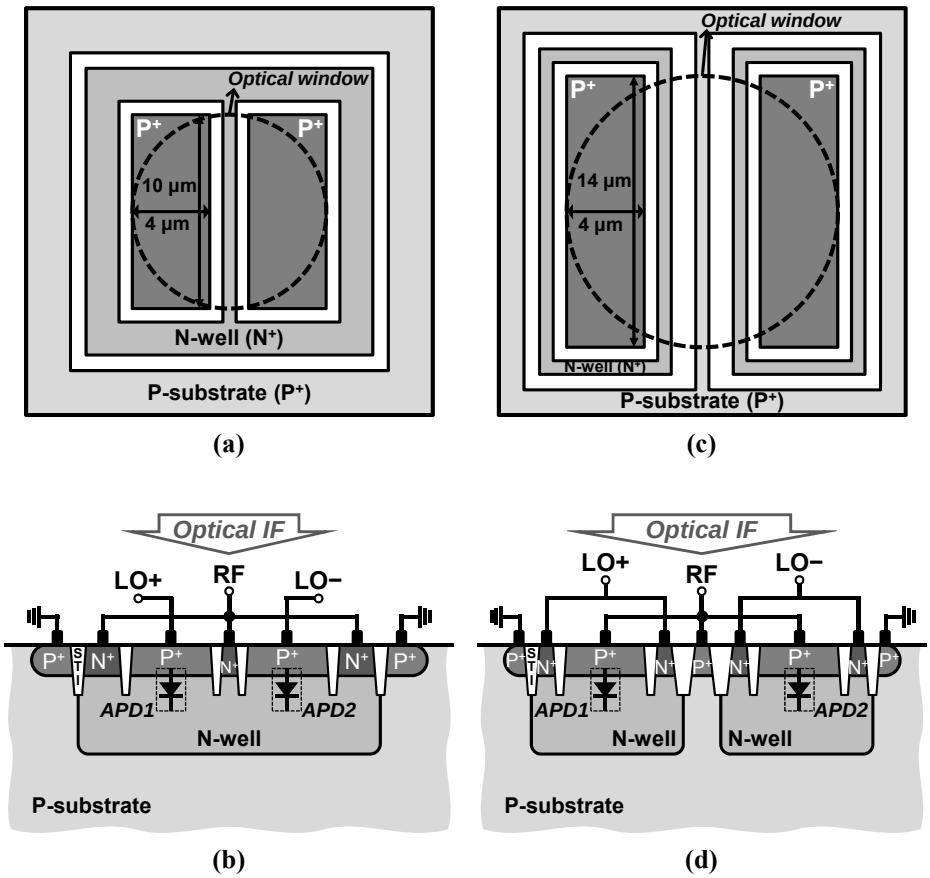

Fig. 3-2-5. Top-view layouts and schematic cross-sections of (a), (b) common-N and (c), (d) common-P balanced SHOEMs.

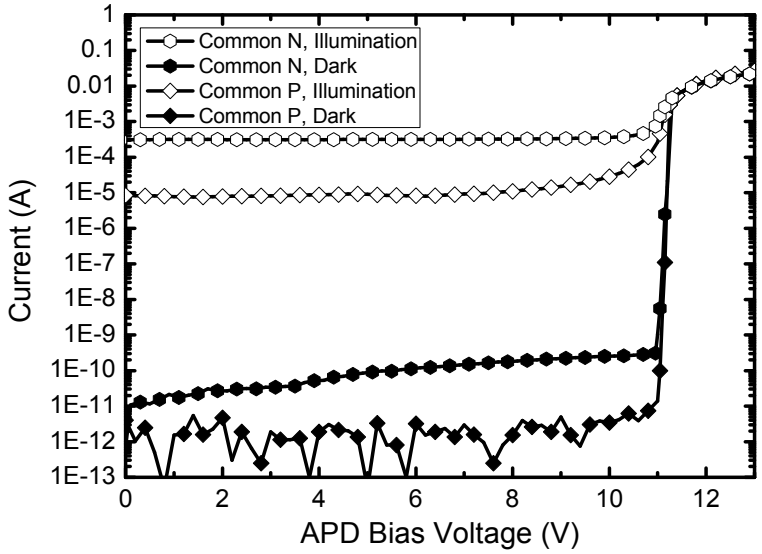

Fig. 3-2-6. Current–voltage characteristics of common-N and common-P balanced SHOEMs.

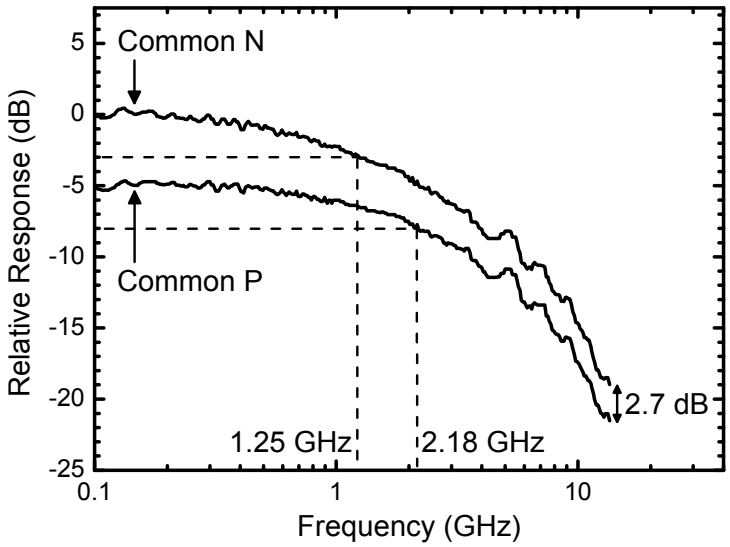

Fig. 3-2-7. Photodetection frequency responses of common-N and common-P balanced SHOEMs.

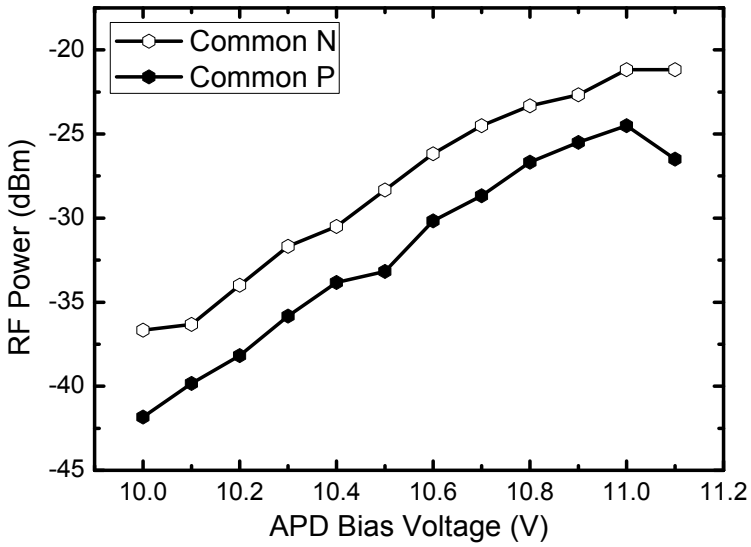

Fig. 3-2-8. 60.1-GHz up-converted RF signal powers of common-N and common-P balanced SHOEMs at different APD bias voltages.

3-2-3. Data Transmission

60-GHz fiber-wireless downlink transmission is demonstrated using the balanced SHOEM. The common-N type is chosen for the balanced SHOEM to maximize up-conversion efficiency. Fig. 3-2-9 shows the experimental setup based on double-sideband self-heterodyne wireless transmission [42]. In self-heterodyne system, the transmitter simultaneously transmits up-converted RF signal and LO signal. Equal power distribution between LO and RF signals maximizes the SNR of received signals. The square-law mixer at the receiver down-converts received RF signal by self-mixing of co-transmitted LO and RF signals without any oscillators. Frequency and phase errors of transmitted LO signal are canceled out. Therefore, self-heterodyne systems enable low-cost and high-quality data transmission without high-performance LOs. In CO, an EOM modulates 850-nm light with 25-Mb/s 32QAM data at 110-MHz carrier generated by a signal generator. Although the photodetection bandwidth of the SHOEM is about 1.25 GHz, relatively small optical IF of 110 MHz is used. This is because there is impedance mismatch between the SHOEM output port and the 60-GHz PA input port. This problem can be solved by adding integrated circuits for impedance matching at the SHOEM.

The modulated optical signals are transmitted to RAU through 4-m-long multimode fiber (MMF). In RAU, transmitted signals are injected into the SHOEM. 30-GHz differential LO signals generated by a signal generator with a 180-degree hybrid are also applied to the SHOEM in an on-wafer probing setup. 60-GHz up-converted RF signals are amplified by a PA having 27.5-dB gain and radiated to mobile terminals using a 24-dBi horn antenna. The inset of Fig. 3-2-9 shows the measured power spectrum of transmitted signals at RAU. Lower-sideband (LSB) and upper-sideband (USB) signals at 59.89 and 60.11 GHz, respectively, are shown in the spectrum. After 1-m wireless transmission, the signals are received by another horn antenna and amplified by an LNA having 18.3-dB gain and 4.8-dB noise figure. Then, they are detected by a Schottky diode.

EVM and SNR performances of recovered data at the output of the mobile terminal are analyzed with a vector signal analyzer. The measured minimum EVM and SNR are 2.4% and 28.6 dB at 11.1-V APD bias, 12-dBm LO, and 0-dBm optical IF. Power spectrum and constellation of output data at this condition are shown in Fig. 3-2-10. The results indicate 2.7% enhancement in EVM with 8 dB lower LO power, compared to the link using the single SHOEM reported in [20].

Fig. 3-2-11 (a) shows EVM and SNR versus LO powers. Increasing

LO power enhances frequency conversion efficiency of the SHOEM and improves EVM and SNR because the link noise is dominated by avalanche photodetection and not influenced by LO power. With LO power over 12 dBm, however, EVM and SNR begin to degrade. This is caused by increase in currents with higher LO power which shifts the APD bias away from the optimum. The results show that LO power can be reduced to 2 dBm for 5% EVM, which is a reasonable requirement for many applications. For example, 64QAM modulation specified in 60-GHz WLAN standardization requires 5.6% EVM [2]. Such LO powers can be achieved with silicon integrated 30-GHz oscillators.

EVM and SNR versus optical IF power are shown in Fig. 3-2-11 (b). The link performance degrades as optical IF power decreases because the output SNR of the SHOEM is reduced. However, improvement in EVM and SNR with increasing optical IF power saturates at about -10-dBm optical IF power. This is due to the nonlinearities in the link caused by the EOM. For 5% EVM, optical input sensitivity is about -15 dBm. With this sensitivity, this scheme can be used up to several kilometers of MMF having, for example, attenuation of 2.3 dB/km and effective modal bandwidth of 4700 MHz·km as is the case for Corning ClearCurve multimode fiber.

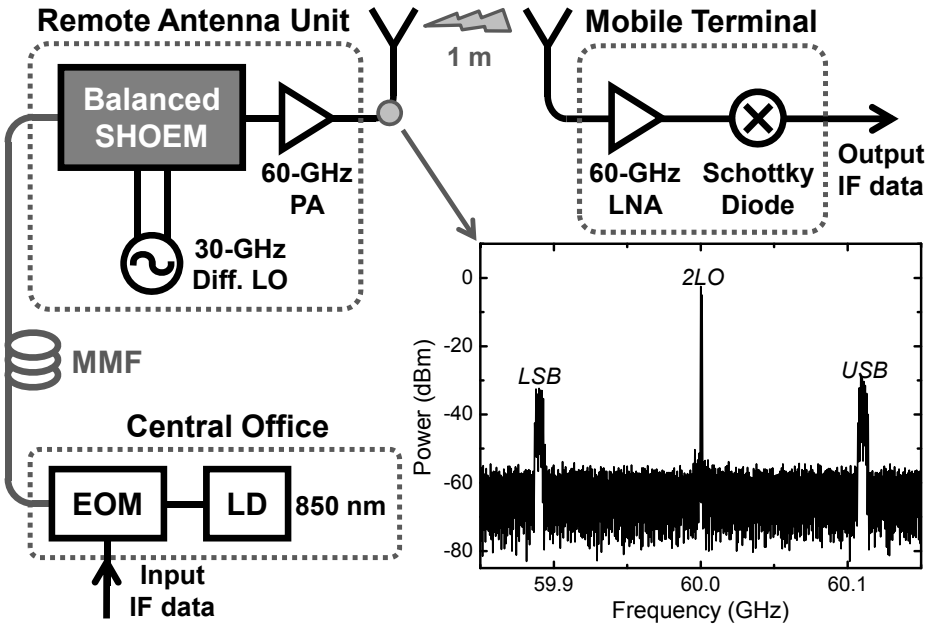

Fig. 3-2-9. Experimental setup for 60-GHz fiber-wireless downlink based on double-sideband self-heterodyne wireless transmission. The inset shows measured power spectrum of transmitted signals at RAU.

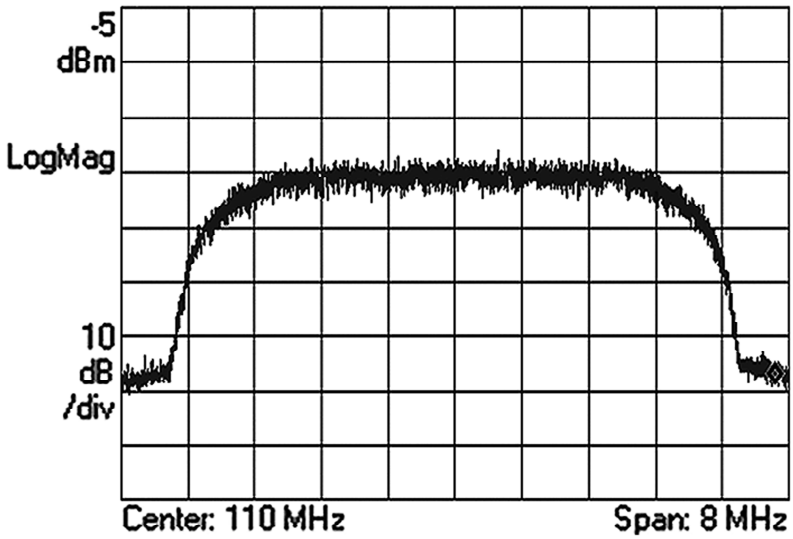

(a)

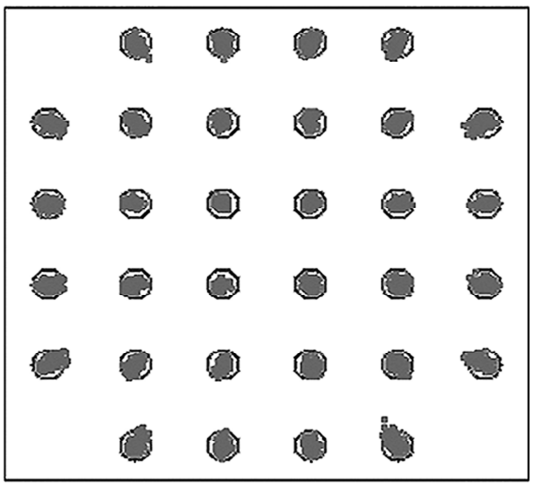

(b)

Fig. 3-2-10. (a) Power spectrum and (b) constellation of output IF data at the reverse bias voltage of 11.1 V, the LO power of 12 dBm, and the optical IF power of 0 dBm.

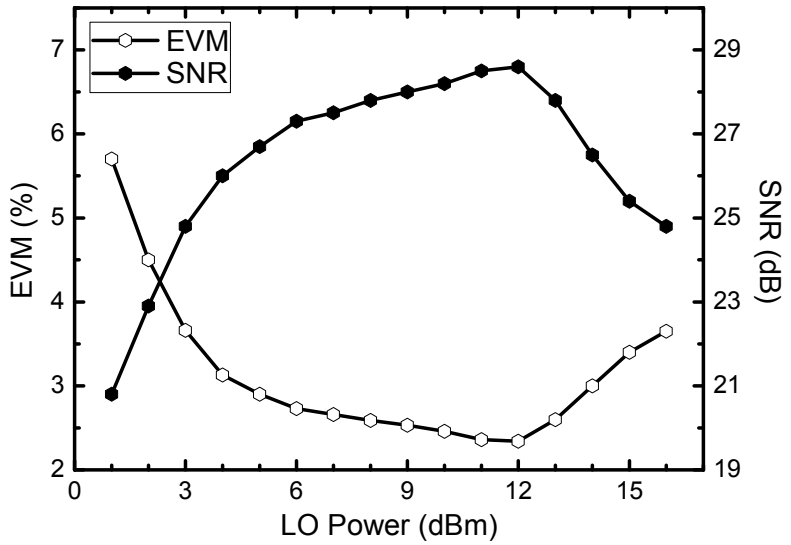

(a)

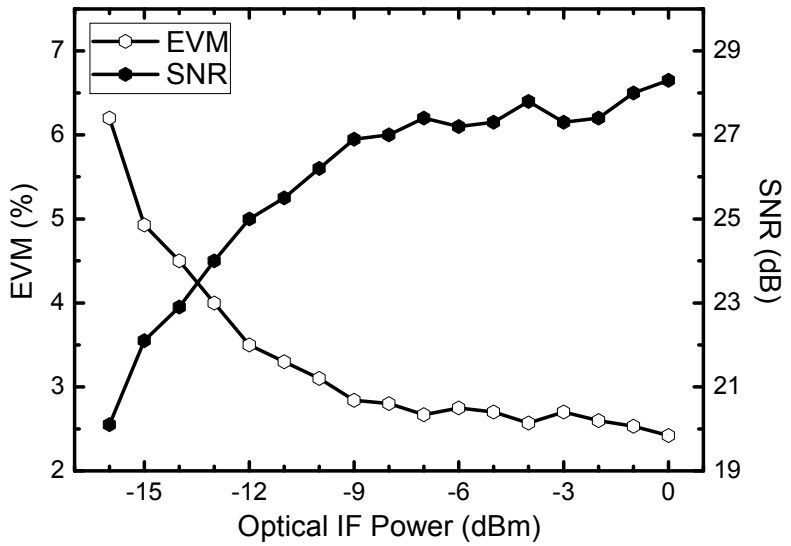

(b)

Fig. 3-2-11. EVM and SNR (a) versus LO power at 0-dBm optical IF power and (b) versus optical IF power at 12-dBm LO power.

3-3. Approach II – Integrated Baseband Photoreceiver and Millimeter-Wave Transmitter: Circuit Implementation

The 60-GHz silicon PWI IC for baseband-over-fiber RAU is divided into two parts, which are a baseband photoreceiver and a 60-GHz transmitter [37]. The baseband photoreceiver is composed of an APD, a TIA, and a VGA. On the other hand, the 60-GHz transmitter consists of a 60-GHz BPSK modulator and a 60-GHz PA. The entire circuit is integrated in a single substrate with IHP's 250-nm SiGe:C BiCMOS technology [41].

Table 3-1 shows power budget for the optical input power range from −10 to 0 dBm. The VGA gain rage is set to 20 dB to maintain PWI IC output power. Gain of each stage, which is TIA, VGA, and 60-GHz Tx, is set to 70 dBΩ, −10 to 10 dB, and 15 dB for 5-dBm output power. Linearity of each stage is carefully considered to handle the expected power from the budget.

Table 3-1
Power budget for 60-GHz PWI IC.

	GAIN	POWER
Optical Input Power	-	**−10 to 0 dBm**
PD Responsivity	0.1 A/W	-
Photodetected Current	-	−100 to −80 dBA_{pk}
TIA Gain	**70 dBΩ**	-
TIA Output Voltage		−30 to −10 dBV_{pk}
VGA Gain	**−10 to 10 dB**	
VGA Output Voltage		−20 dBV_{pk}
60-GHz Tx Conversion Gain	**15 dB**	
PA Output Voltage	-	−5 dBV_{pk}
PA Output Power w/ 50-Ω Load	-	**5 dBm**

3-3-1.Baseband Photoreceiver

The baseband photoreceiver consists of the APD, the TIA with a DC-balanced buffer, and the VGA. The APD uses vertical PN-junction formed between P^+ source/drain region and N-well region having an optical window of 10 μm × 10 μm. This is identical to the APD in CMOS technology mentioned in section 2 since it is realized with CMOS process layers in BiCMOS technology. The APD has the avalanche breakdown voltage of 12.2 V and the maximum responsivity is about 15.4 A/W, and its maximum 3-dB photodetection bandwidth is about 3.5 GHz [43].

Fig. 3-3-1 shows the schematics of the TIA and the following DC-balanced buffer. As shown in Fig. 3-3-1 (a), the TIA consists of a two-stage common-source differential amplifier with 3.1-kΩ shunt feedback resistors R_F. Even though input light is single-ended, another dummy APD is used to deliver symmetric impedance to the differential TIA input. Fig 3-3-1 (b) depicts the DC-balanced buffer composed of an LPF and a f_T-doubler amplifier. This buffer is added after the TIA and converts pseudo-differential TIA output into fully differential [44]. The cut-off frequency of the LPF is set to 1 MHz in order to prevent any DC wander. Fig. 3-3-2 shows the simulated transimpedance gain and

input-referred noise current of the TIA with the DC-balanced buffer. For simulations, the equivalent circuit model of the APD is developed in the same manner discussed in section 2-3. The transimpedance gain shown in Fig. 3-3-2 (a) is plotted at two conditions whether the model considers the transit time effect or not. The simulated gain at low frequencies is about 68 dBΩ. And the 3-dB photodetection bandwidth is about 4.7 GHz without the transit time effect, but it diminishes to 2.7 GHz with the transit time effect. Thus, the APD is the bandwidth limiting block as all other blocks can have wider bandwidth with high-speed design. The input noise current shown in Fig. 3-3-2 (b) is 4.5 pA/√Hz at low frequencies and 0.317 μA_{rms} accumulated within the bandwidth of 2.7 GHz.

Fig. 3-3-3 shows the schematic of the VGA which is a two-stage amplifier with MOS emitter-degeneration variable resistors [45]. The gain is varied by changing the on-resistance of the MOS with the gain control voltage V_{CTRL}. Fig. 3-3-4 (a) shows the simulated low-frequency transimpedance gain of the baseband photoreceiver measured at the VGA output as a function of the gain control voltage. The gain range is 20 dB from −10 to 10 dB as the gain control voltage varies from 1.9 to 2.3 V. The gain at different VGA gains as a function of frequency is shown in Fig. 3-3-4 (b). The bandwidth at the 10-dB VGA gain is about

2.57 GHz, and the bandwidth increases as the VGA gain decreases. This is because gain control is realized by reducing DC gain by emitter degeneration.

Power consumption of the TIA and the VGA including bias circuits is 27.7 and 23.7 mW at a 2.5-V supply, respectively.

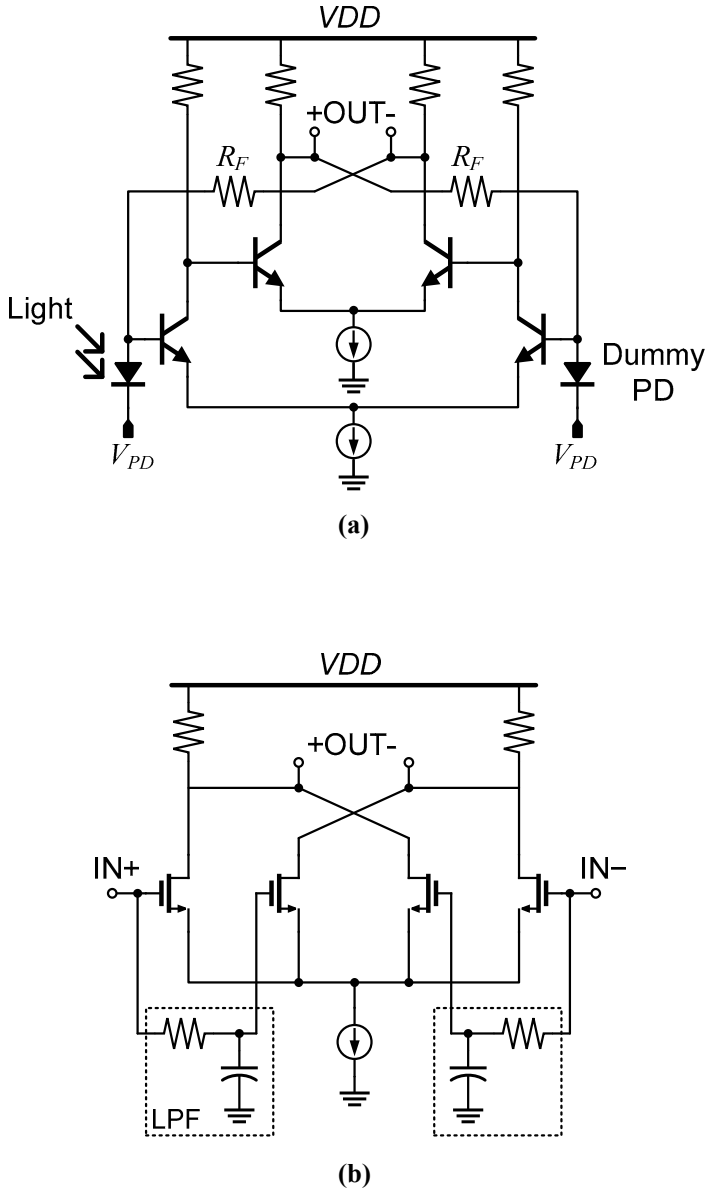

Fig. 3-3-1. Schematics of (a) TIA and (b) DC-balanced buffer in standard BiCMOS technology.

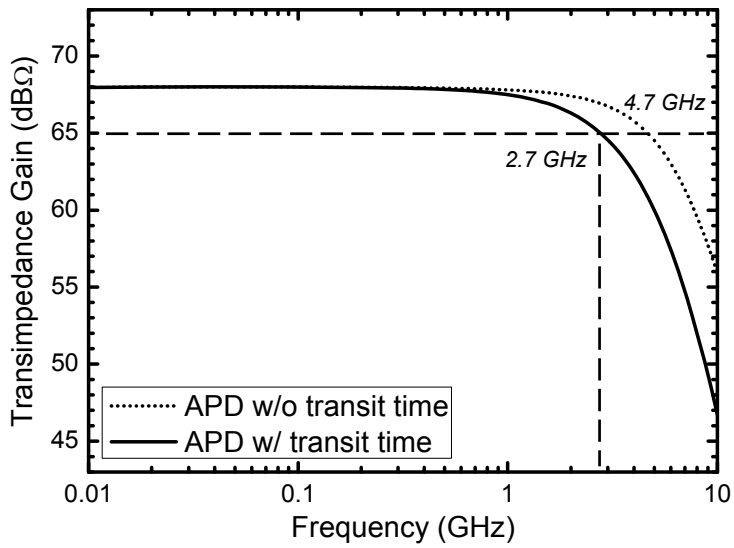

(a)

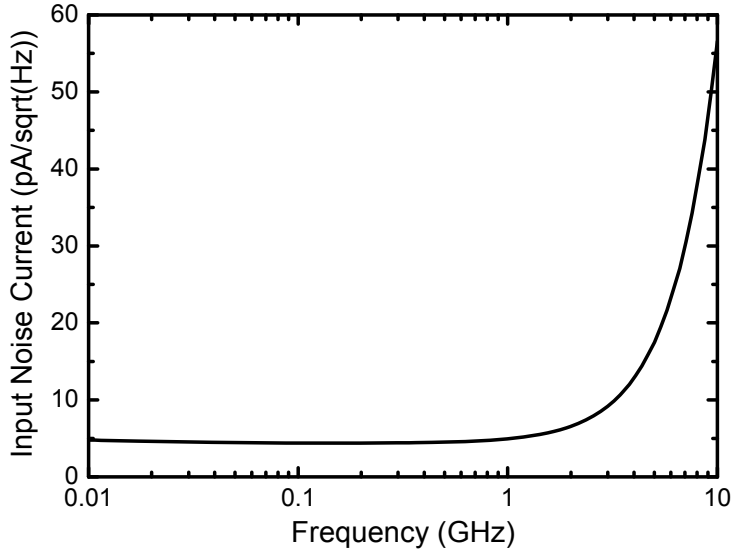

(b)

Fig. 3-3-2. Simulated (a) transimpedance gain and (b) input noise current of TIA with DC-balanced buffer as a function of frequency.

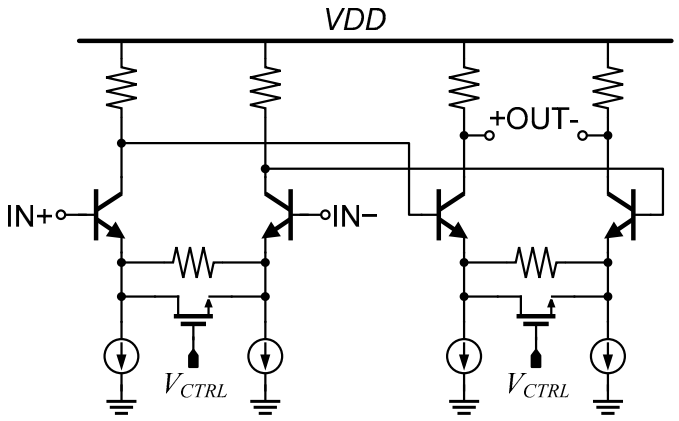

Fig. 3-3-3. Schematic of VGA in standard BiCMOS technology.

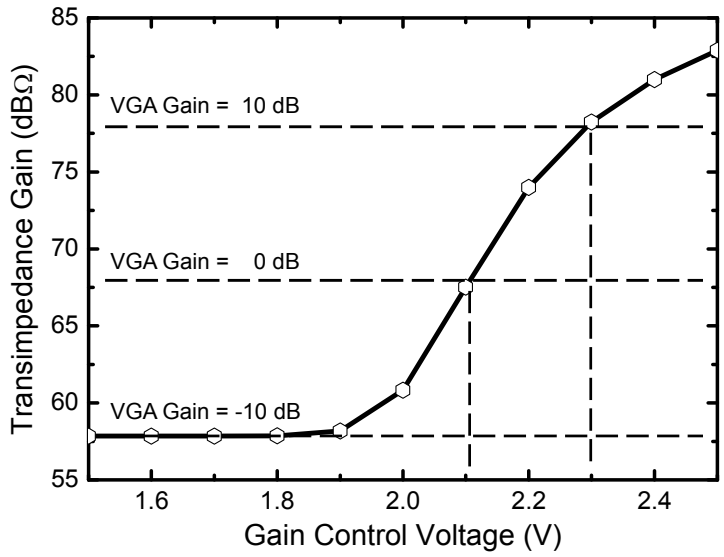

(a)

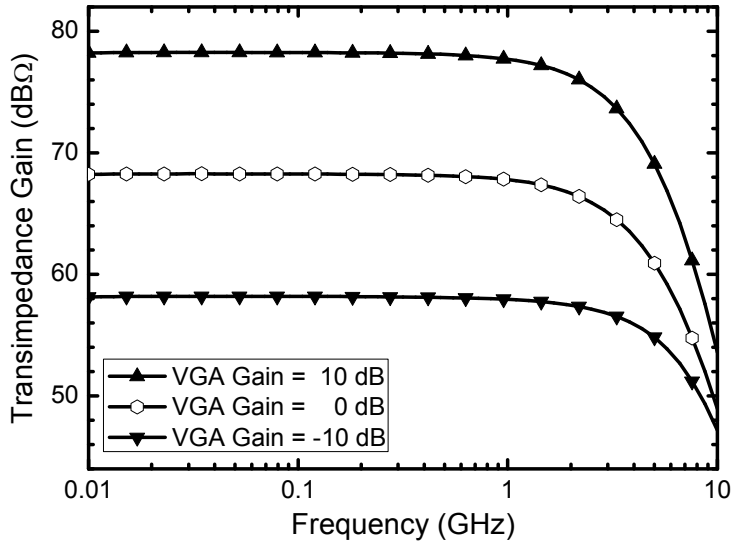

(b)

Fig. 3-3-4. Simulated transimpedance gain of baseband photoreceiver at VGA output as a function of (a) gain control voltage at low frequency and (b) frequency at VGA gain of –10, 0, and 10 dB.

3-3-2.Millimeter-Wave Transmitter

The millimeter-wave transmitter is composed of the 60-GHz BPSK modulator and the 60-GHz PA. Fig. 3-3-5 (a) shows the schematic of the 60-GHz BPSK modulator in BiCMOS technology. The modulator is a double-balanced Gilbert-cell mixer with 60-GHz differential LO input. A balun is used as a load inductor to convert differential modulator output signals into single-ended signals for PA input. Fig. 3-3-5 (b) shows the schematic of the 60-GHz PA which is a one-stage single-ended cascode amplifier. It has an emitter-degeneration inductor to ensure stable operation. And the output impedance of the PA is tuned to maximize the power delivered to the off-chip 50-Ω load by using load-pull simulation.

Fig. 3-3-6 (a) shows the simulated voltage conversion gain of the 60-GHz transmitter at different LO frequencies with the IF frequency of 100 MHz and the LO power of 3 dBm. Since the BPSK modulator is a double-sideband modulator, the conversion gain for lower-sideband $f_{LO} - f_{IF}$, upper-sideband $f_{LO} - f_{IF}$, and both-sideband component, which is the sum of two sidebands, are plotted. The peak gain for the both sideband is about 15.8 dB at 55 GHz. The peak frequency is below than intended and this is caused by a mistake in design. However, the 3-dB

bandwidth is over 14 GHz from 50 to 64 GHz. Fig. 3-3-6 (b) shows the voltage conversion gain at different IF frequencies with LO frequency and power of 59 GHz and 3 dBm. Due to the lowered peak frequency, the responses of two sidebands are non-symmetric and the upper-sideband response has lower 3-dB bandwidth of 6 GHz. The bandwidth of the both sideband is about 8.9 GHz. This indicates the IF bandwidth is limited by the baseband photoreceiver, not by the 60-GHz transmitter.

Fig. 3-3-7 shows the simulated both-sideband output power as a function of the input voltage. The output 1-dB compression point is 9.5 dBm at the input voltage of -13.8 dBV. The output return loss at the PA output is below –10 dB from 53.3 to 64 GHz as shown in Fig. 3-3-8. The LO leakage at the PA output is below –19 dBm. Power consumption of the BPSK modulator and the PA is 44.7 and 67.2 mW at a 3-V supply, respectively.

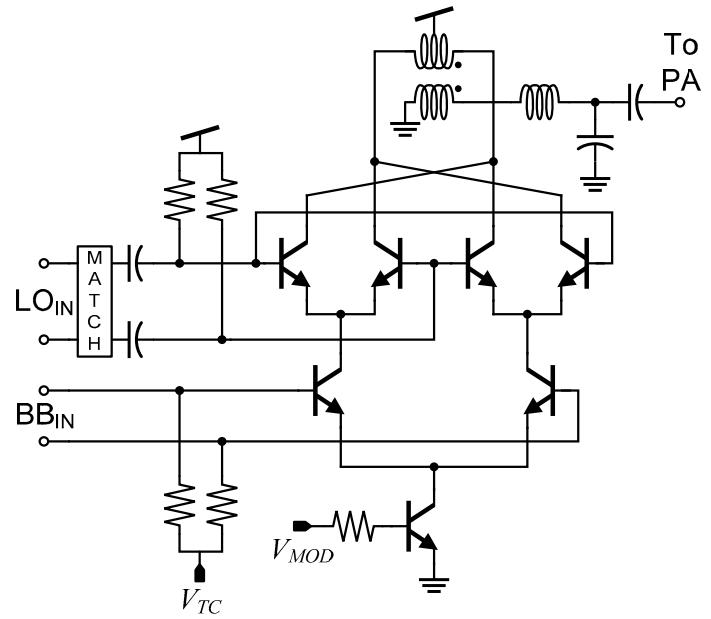

(a)

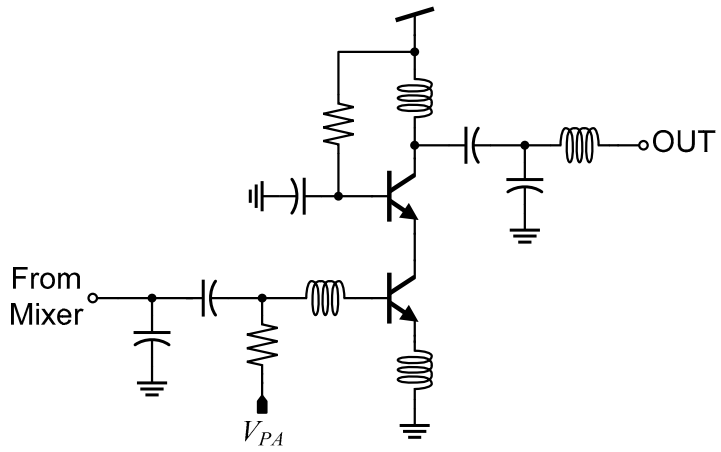

(b)

Fig. 3-3-5. Schematic of (a) 60-GHz BPSK modulator and (b) 60-GHz PA in standard BiCMOS technology.

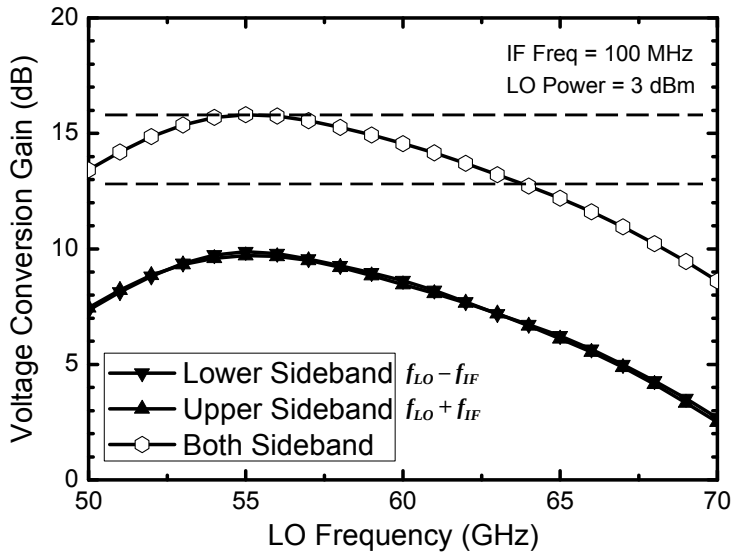

(a)

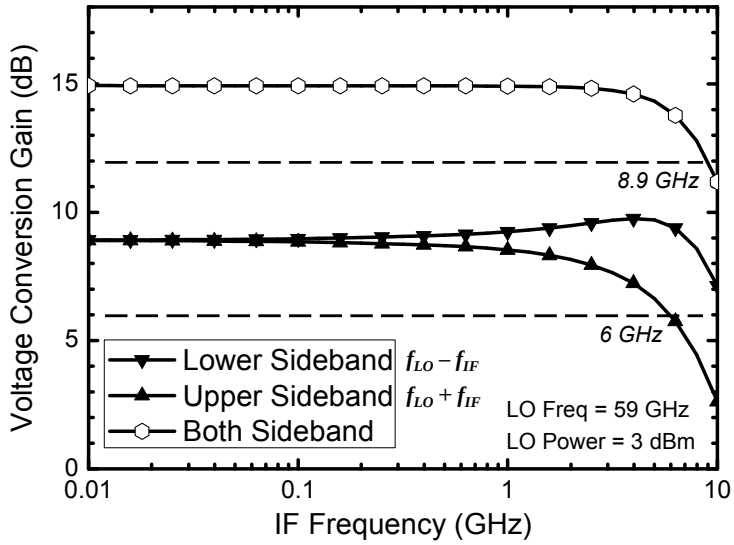

(b)

Fig. 3-3-6. Simulated voltage conversion gain of 60-GHz transmitter at (a) different LO frequencies and (b) different IF frequencies.

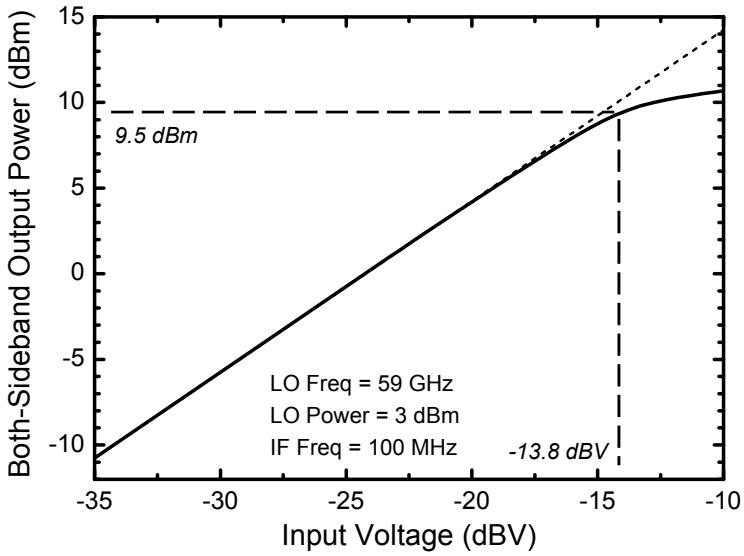

Fig. 3-3-7. Simulated both-sideband output power of 60-GHz transmitter as a function of input voltage.

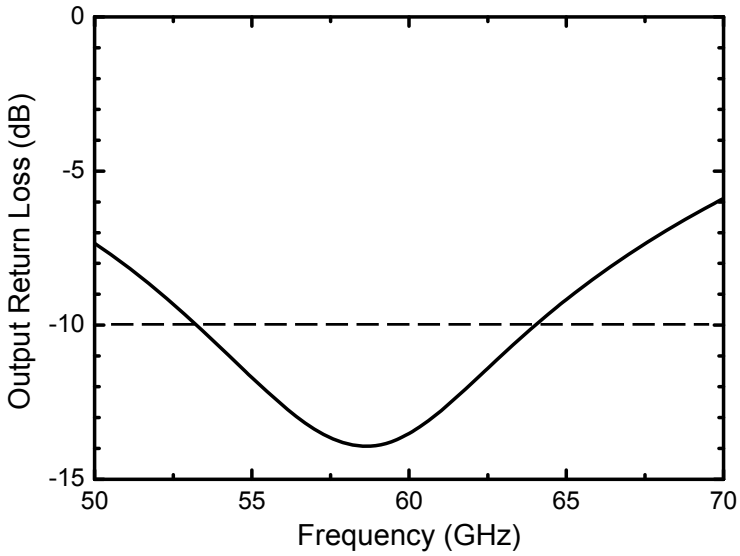

Fig. 3-3-8. Simulated output return loss of 60-GHz transmitter.

3-4. Approach II – Integrated Baseband Photoreceiver and Millimeter-Wave Transmitter: Experimental Results

3-4-1. Circuit Measurement

Fig. 3-4-1 shows the chip photo of the 60-GHz PWI IC. The chip area including all probe pads is 0.5 mm × 1.42 mm. The fabricated chip is characterized by on-wafer probing setup. For characterization, single-tone optical data are injected into the APD with optical input power monitored by an in-line power meter. The resulting 60-GHz up-converted electrical signals are measured by a spectrum analyzer. Measurement loss from probes and cables is deembedded. Fig. 3-4-2 shows up-converted single-sideband output signal powers with optical signal modulated with single-tone frequencies from 200 MHz to 3 GHz under varying VGA gains. For this measurement, 3-dBm 59-GHz LO and −10-dBm optical input signals are used. Measured data show that the PWI IC executes O/E conversion, amplification, and 60-GHz up-conversion. Its frequency response at each VGA gain has a flat response adequate for broadband data modulation.

Fig. 3-4-3 shows the output powers for different optical input powers. For this measurement, 100-MHz optical signal is introduced to the APD

and the total output power including both sidebands of up-converted signals are measured. Output power of 6.8 dBm is achieved at 0-dBm optical input power. Output power compression occurs because of both avalanche gain saturation and PA gain compression.

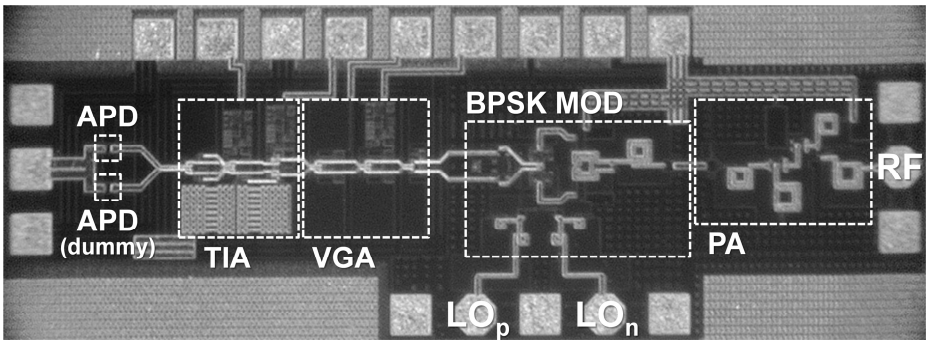

Fig. 3-4-1. Chip photo of 60-GHz PWI IC in standard BiCMOS technology.

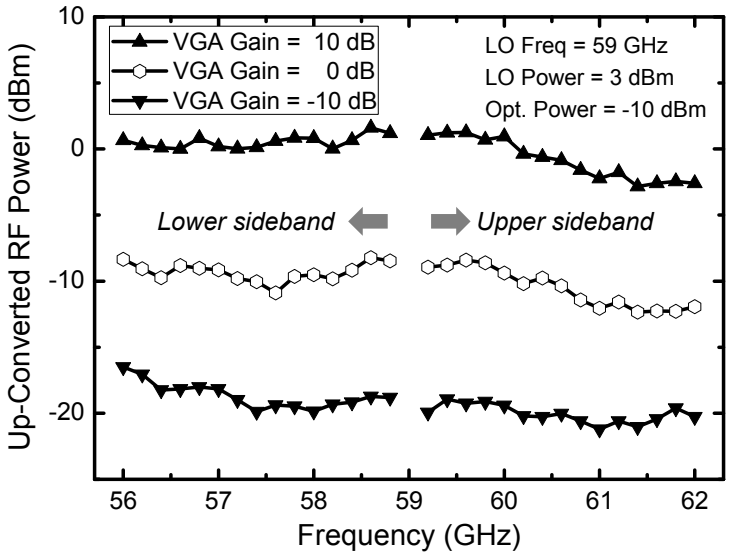

Fig. 3-4-2. Up-converted output RF powers of 60-GHz PWI measured at different optical frequencies and VGA gain.

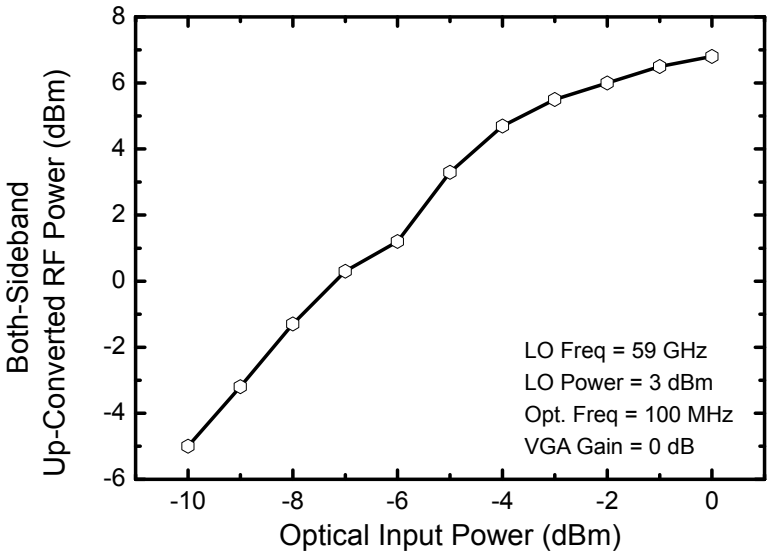

Fig. 3-4-3. Up-converted output total both-sideband RF powers of 60-GHz PWI measured at different optical input power.

3-4-2. Data Transmission

BPSK data transmission in 60-GHz millimeter-wave photonic downlink is demonstrated by using the PWI IC as shown in Fig. 3-4-4. In a central office, an electro-optic modulator modulates 850-nm light from a laser diode with 1.6-Gb/s 2^7-1 pseudo-random binary sequence (PRBS) data from a pattern generator. The modulated optical signals are transmitted to the RAU through 4-m multimode fiber, and they are injected into the PWI IC by using 10-μm-diameter lensed fiber. Differential LO signals are generated from a 180-degree hybrid and a 60-GHz signal generation unit composed of an active frequency doubler and a 30-GHz signal generator. The LO frequency of 59 GHz is experimentally chosen for the best transmission performance. The PWI IC converts the optical signals into BPSK-modulated electrical signals with 59-GHz carrier as shown in the inset of Fig. 3-4-4. The BPSK signals are transmitted to the mobile terminal via 2-m wireless channel using a 24-dBi horn antenna at each side. The mobile terminal consists of an LNA, a mixer, an LO signal generator, and a BPSK demodulator. The demodulator is a custom-designed IC and it provides demodulation up to 1.6 Gb/s [46]. The LO frequency of 55.715 GHz is used for down-conversion because the demodulator has the best performance at

the carrier frequency of 3.285 GHz. The demodulated data are analyzed by a BER tester. Testing with longer PRBS pattern length than 2^7-1 is required in order to make sure the PWI IC does not suffer from pattern-dependent problems, but this was not possible due to the long-term reliability of our demodulator.

Fig. 3-4-5 (a) shows the measured BERs versus optical input powers injected into the PWI IC at different VGA gains. As the gain increases by 5 dB, the required input power for the same BER lessens by about 2.5 dB, equivalent to O/E-converted electrical power of 5 dB. It indicates that the SNR is limited by the wireless link after the VGA stage, not by the photonic link. This enhancement is desensitized at the 10-dB gain because the large gain increases noise from the photonic link, thus affecting SNR. On the other hand, the large VGA gain causes a nonlinearity problem of the wireless link components, especially the BPSK modulator and the PA, degrading the BER performance at large input powers. Therefore, the VGA gain should be controlled according to the input power level. The minimum input power for BER of 10^{-6} is −10 dBm and for error-free operation is −6 dBm. Eye diagrams of demodulated data for these two conditions are shown in Fig. 3-4-6. Thick transition lines are due to intrinsic timing errors in the demodulator [46].

Fig. 3-4-5 (b) shows the BER performance at different APD bias voltages. As the bias increases, the APD avalanche gain also increases until the bias reaches 14.5 V, which is the maximum avalanche gain point. Increasing avalanche gain enhances BER at small input powers. However, it cannot handle large input powers because additional DC currents induced by optical input signals push the APD bias away beyond the avalanche breakdown. Therefore, the APD bias should be carefully controlled for achieving wide dynamic range.

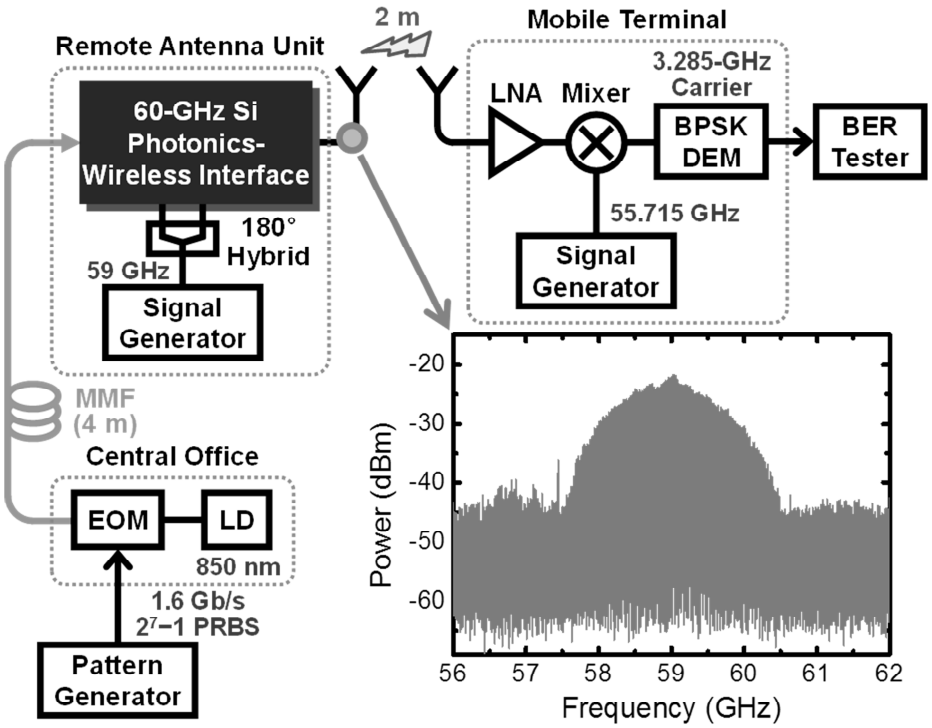

Fig. 3-4-4. Experimental setup for 1.6-Gb/s BPSK data transmission in 60-GHz millimeter-wave photonic downlink using 60-GHz PWI. Inset shows measured power spectrum of transmitted signals with 59-GHz carrier at RAU.

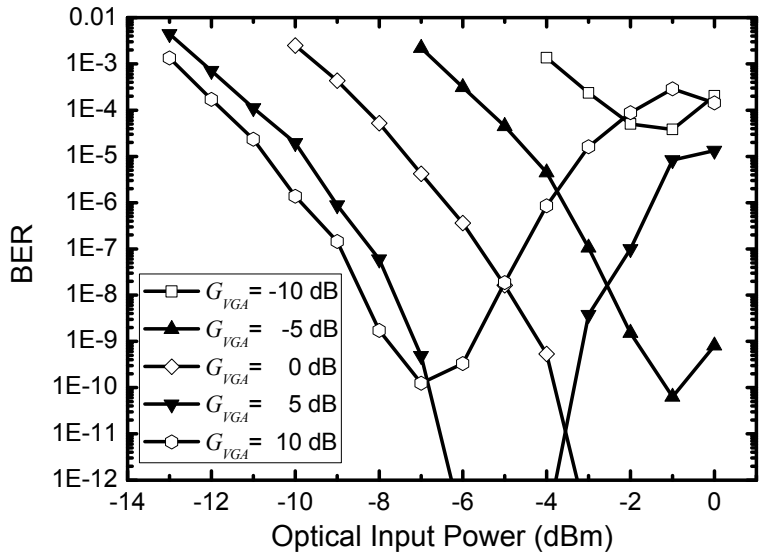

(a)

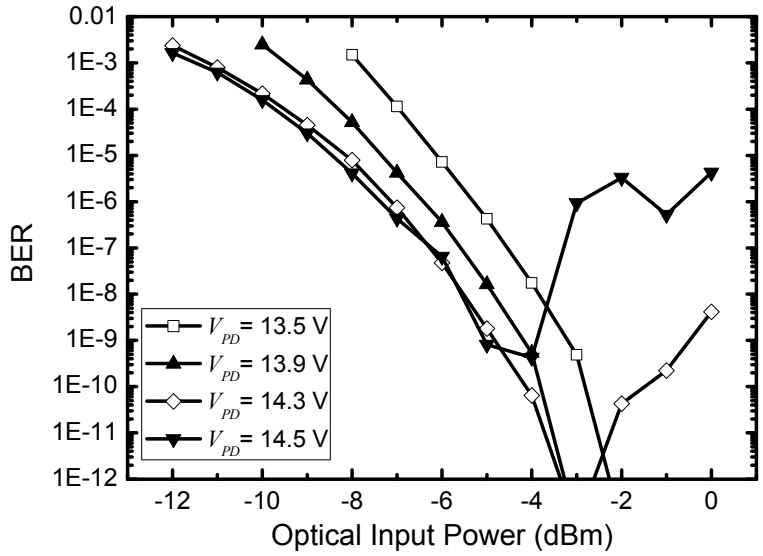

(b)

Fig. 3-4-5. BER versus optical input powers at (a) different VGA gains (G_{VGA}) and (b) different APD bias voltages (V_{PD}).

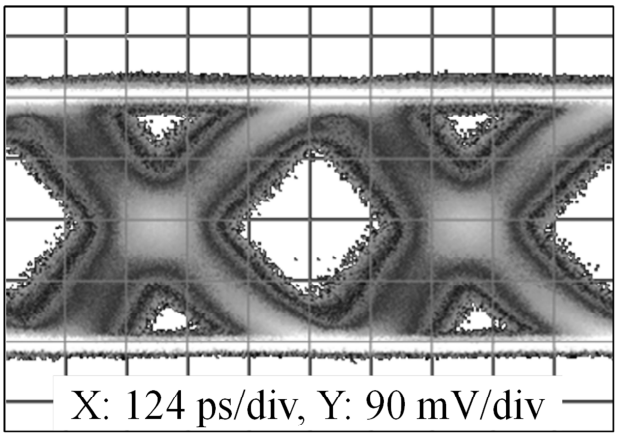

(a)

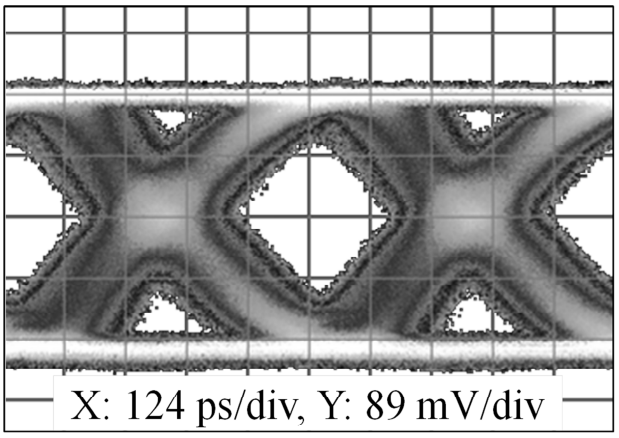

(b)

Fig. 3-4-6. Eye diagram of demodulated data for (a) 10^{-6} BER and (b) error-free.

3-5. Summary

Two kinds of 60-GHz PWI ICs are developed for IF-over-fiber and baseband-over-fiber fiber-wireless networks, respectively. A new type of SHOEM using a balanced APD pair is introduced for enhanced conversion efficiency. This IF-over-fiber PWI IC will be very useful for low-cost application using self-heterodyne system. As a baseband-over-fiber PWI IC, an integrated baseband photoreceiver and 60-GHz transmitter IC also shows a great potential for realizing cost-effective RAUs. It receives optical data and converts them into 60-GHz BPSK signals in a single silicon chip. It has the optical input sensitivity of −10 dBm and 60-GHz output power of 6.8 dBm. Design and demonstration results of the 60-GHz baseband-over-fiber PWI IC are summarized in Table 3-2.

Table 3-2
Performance summary of 60-GHz PWI IC.

DESIGN RESULTS	
Technology	250-nm SiGe:C BiCMOS
Photodetector	P^+/N-well APD (10 μm × 10 μm)
Frequency	59 GHz
Transimpedance Conversion Gain (simulation)	73 – 93 dBΩ (variable) at 59-GHz 3-dBm LO and 100-MHz IF
60-GHz Output Power At Optical Input Power	–5 dBm at –10 dBm 6.8 dBm at 0 dBm
Output 1-dB Compression Point	6.8 dBm
Power Consumption Baseband Photoreceiver 60-GHz Transmitter	 51.4 mW at 2.5-V supply 111.9 mW at 3-V supply
Chip Area	0.5 mm × 1.42 mm
DEMONSTRATION RESULTS	
Data Rate	1.6-Gb/s BPSK
Frequency	59 GHz
Wireless Distance	2 m
Optimum Optical Input Power	−10 dBm for 10^{-6} BER
Optimum APD Bias Voltage	13.9 V
Minimum BER	Error free at −6-dBm optical power

4. Conclusion

Fiber-wireless network has come into the spotlight as mobile users have been demanding increasingly higher data throughput and wider usage coverage. The picocells should be densely configured with enormous RAUs to meet the requirements, and consequently, network implementation cost is significantly influenced by RAU cost.

This dissertation aimed at low-cost realization of RAU for future fiber-wireless network based on electronic-photonic integrated circuit on a single silicon platform. Three different RAU architectures depending on optical data distribution schemes which are RF-over-fiber, IF-over-fiber, and baseband-over-fiber schemes were considered, and PWI ICs for each of RAUs were realized with standard silicon technology.

Silicon APDs used for PWI ICs were characterized with DC, optoelectronic frequency response, and S-parameter measurements to develop an equivalent circuit model for PWI IC design. APD shot noise characteristic was also measured for investigating optimal SNR design.

The 5-GHz PWI IC consisting of APD, preamplifier, and PA for RF-over-fiber RAU was developed with standard 180-nm CMOS technology. Low-noise design was achieved by noise matching

technique between APD and preamplifier and proper APD biasing for maximum SNR. Demonstration of 54-Mb/s WLAN data transmission in 5-GHz fiber-wireless downlink utilizing the PWI IC achieved good optical input sensitivity of –13 dBm for 5.6% EVM specified in IEEE 802.11 standards.

The 60-GHz balanced SHOEM based on APD pair was investigated for IF-over-fiber PWI IC. It receives IF optical signals and converts them into 60-GHz signals simultaneously. This study focused on the device optimization by comparing common-N and common-P pairs. The comparison results show that common-N pair has higher conversion efficiency and common-P pair has wider photodetection bandwidth. Data transmission in 60-GHz fiber-wireless network was performed by utilizing the balanced SHOEM based on common-N APD pair. The demonstration shows great improvement in optical input sensitivity and LO input power compared to previously reported single SHOEM.

The 60-GHz PWI IC containing APD, TIA with DC-balanced buffer, VGA, 60-GHz BPSK modulator, and PA for baseband-over-fiber RAU was developed with standard 250-nm SiGe BiCMOS technology. It can convert optically modulated baseband data into 60-GHz BPSK signals with enough amplification in a single chip. PWI IC performance was

verified with 1.6-Gb/s BPSK data transmission. BER performance can be optimized by changing APD bias and VGA gain and optimum optical input sensitivity of –10 dBm for 10^{-6} BER was obtained.

The PWI ICs in this dissertation are limited to downlink 850-nm applications as standard silicon technology provides silicon PDs for 850-nm wavelength and no waveguide structures required for modulators. Nevertheless, they validate the feasibility of applying silicon electronic-photonic integrated circuit technology for implementing compact and low-cost RAUs in future fiber-wireless network.

Bibliography

[1] IEEE Std 802.15.3c-2009, Sep. 11, 2009

[2] *Task Group*, IEEE 802.11ad.

[3] J. Capmany and D. Novak, "Microwave photonics combines two worlds," *Nature Photonics*, vol. 1, pp. 319–330, June 2007.

[4] N. J. Gomes, A. Nkansah, and D. Wake, "Radio-Over-MMF Techniques—Part I: RF to Microwave Frequency Systems," *J. Lightwave Technol.*, vol. 26, no. 15, pp. 2388–2395, Aug. 2008.

[5] A. M. J. Koonen and M. G. Larrodé, "Radio-Over-MMF Techniques—Part II: Microwave to Millimeter-Wave Systems," *J. Lightwave Technol.*, vol. 26, no. 15, pp. 2396–2408, Aug. 2008.

[6] C. Lim *et* al., "Fiber-Wireless Networks and Subsystem Technologies," *J. Lightwave Technol.*, vol. 28, no. 4, pp. 390–405, Feb. 2010.

[7] H.Ogawa, D. Polifko, and S. Banba, "Millimeter-Wave Fiber Optics Systems for Personal Radio Communication," *IEEE Trans. Microw. Theory Tech.*, vol. 40, no. 12, pp. 2285–2293, Dec. 1992.

[8] M. Weiß *et al*., "60-GHz Photonic Millimeter-Wave Link for Short- to Medium-Range Wireless Transmission Up to 12.5 Gb/s," *J. Lightwave Technol.*, vol. 26, pp. 2424–2429, Aug. 2008.

[9] I. Haroun *et al*., "Multi-band 700MHz/ 2.4GHz/ 60GHz RF Front-End for Radio-over-Fiber Base Stations," in *Proc. 2010 IEEE Radio and Wireless Symposium*, pp. 629–632, Jan. 2010.

[10] M. Maier, N. Ghazisaidi and M. Reisslein, “The Audacity of Fiber-Wireless (FiWi) Networks,” in *Lecture Notes of the Institute for Computer Sciences, Social Informatics and Telecommunications Engineering*, vol. 6, pp. 16–35, 2009.

[11] A. M. Niknejad, “Siliconization of 60 GHz,” *IEEE Microwave Magazine*, vol.11, pp.78–85, Feb. 2010.

[12] B. Razavi, “Design of Millimeter-Wave CMOS Radios: A Tutorial,” *IEEE Trans. Circuits and Syst. I*, vol. 56, pp. 4–16, Jan. 2009.

[13] C. Marcu *et al.*, “A 90 nm CMOS Low-Power 60 GHz Transceiver With Integrated Baseband Circuitry,” *IEEE J. Solid-State Circuits*, vol.44, no.12, pp.3434–3447, Dec. 2009.

[14] S. Glisic *et al.*, “A Fully Integrated 60 GHz Transmitter Front-End in SiGe BiCOMS Technology,” in *Proc. 11th Topical Meeting on Silicon Monolithic Integrated Circuits in RF Systems*, pp. 149–152, Jan. 2011.

[15] M. Hochberg *et al.*, “Silicon Photonics: The Next Fabless Semiconductor Industry,” *IEEE Solid-Stage Circuits Mag.*, vol. 5, no. 1, pp. 48–58, Mar. 2013.

[16] L. Vivien *et al.*, “42 GHz waveguide Germanium-con-silicon vertical PIN photodetector,” in *Proc. 5th Int. Conf. Group IV Photonics,* pp. 185–187, Sep. 2008.

[17] S. Assefa *et al.*, “CMOS-Integrated 40GHz Germanium Waveguide Photodetector for On-chip Optical Interconnects,” in *Proc. OFC/NFOEC 2009*, paper OMR4, Mar. 2009.

[18] L. Liao *et al.*, “40 Gbit/s silicon optical modulator for high-speed applications,” *Electron. Lett.*, vol. 43, no. 22, pp. 1196–1197, Oct. 2007.

[19] G. Li *et al.*, “40 Gb/s thermally tunable CMOS ring modulator,” in *Proc. 9th Int. Conf. Group IV Photonics,* pp. 1–3, Aug. 2012.

[20] H.-S. Kang and W.-Y. Choi, “Fibre-supported 60 GHz self-heterodyne systems based on CMOS-compatible harmonic optoelectronic mixers,” *Electron. Lett.*, vol. 43, no. 20, pp. 1101–1103, Sep. 2007.

[21] M. Ko *et al.*, “A Silicon Balanced Subharmonic Optoelectronic Mixer for 60-GHz Fiber-Wireless Downlink Application,” *IEEE Photonics Technol. Lett.*, vol. 23, no. 23, pp. 1805–1807, Dec. 2011.

[22] W.-Z. Chen and S.-H. Huang, “A 2.5 Gbps CMOS Fully Integrated Optical Receiver With Lateral PIN Detector,” in *Proc. IEEE Custom Integrated Circuits Conf.*, pp. 293–296, Sep. 2007.

[23] S.-H. Huang *et al.*, “A 10-Gb/s OEIC With Meshed Spatially-Modulated Photo Detector in 0.18-μm CMOS Technology,” *IEEE J. Solid-State Circuits*, vol. 46, no. 5, pp. 1158–1169, May 2011.

[24] M.-J. Lee and W.-Y. Choi, “A silicon avalanche photodetector fabricated with standard CMOS technology with over 1 THz gain-bandwidth product,” *Opt. Express*, vol. 18, no. 23, pp. 24189–24194, Nov. 2010.

[25] M. Ko *et al.*, “5-GHz CMOS Integrated Radio-Over-Fiber Receiver,” in *Proc. Asia-Pacific Microw. Conf. 2013*, paper PA-4, Apr. 2013.

[26] M.-J. Lee, H.-S. Kang, and W.-Y. Choi, “Equivalent Circuit Model for Si Avalanche Photodetectors Fabricated in Standard CMOS Process,” *IEEE Electron Device Lett.*, vol. 29, no. 10, pp. 1115–1117, Oct. 2008.

[27] A. Leven, R. Reuter, and Yves Baeyens, “Unified Analytical Expressions for Transimpedance and Equivalent Input Noise Current of Optical Receivers,” *IEEE Trans. Microw. Theory Tech.*, vol. 48, no. 10, pp. 1701–1706, Oct. 2000.

[28] A. Leven *et al.*, “Design of Narrow-Band Photoreceivers by Means of the Photodiode Intrinsic Conductance,” *IEEE Trans. Microw. Theory Tech.*, vol. 49, no. 10, pp. 1908–1913, Oct. 2001.

[29] G. Gonzalez, *Microwave Transistor Amplifiers: Analysis and Design*, 2nd ed., Upper Saddle River, NJ: Prentice Hall, 1997.

[30] M.-J. Lee and W.-Y. Choi, “Performance Comparison of Two Types of Silicon Avalanche Photodetectors Based on N-well/P-substrate and P^+/N-well Junctions Fabricated With Standard CMOS Technology,” *J. Opt. Soc. Korea*, vol. 15, no. 1, pp. 1–3, Mar. 2011.

[31] M.-J. Lee and W.-Y. Choi, “Area-Dependent Photodetection Frequency Response Characterization of Silicon Avalanche Photodetectors Fabricated With Standard CMOS Technology,” *IEEE Trans. Electron Devices*, vol. 60, no. 3, pp. 998–1004, Mar. 2013.

[32] T. E. Kolding, “A Four-Step Method for De-Embedding Gigahertz On-Wafer CMOS Measurements,” *IEEE Trans. Electron. Devices*, vol. 47, no. 4, pp. 734–740, Apr. 2000.

[33] S. M. Sze and K. K. Ng, *Physics of Semiconductor Devices*, 3rd ed., Hoboke, NJ: Wiley, 2007.

[34] T.-K. Nguyen *et al.*, “CMOS Low-Noise Amplifier Design Optimization Techniques,” *IEEE Trans. Microw. Theory Tech.*, vol. 52, no. 5, pp. 1433–1442, May 2004.

[35] IEEE Std 802.11-2007, Mar. 8, 2007.

[36] J.-Y. Kim, “Conversion Efficiency Enhancement of Millimeter-wave Optoelectronic Mixers for Fiber-fed Wireless System,” Ph.D. dissertation, Dept. Elect. Electron. Eng., Yonsei Univ., Seoul, Korea, 2011.

[37] M. Ko *et al.*, “Silicon Photonics-Wireless Interface IC for 60-GHz Wireless Link,” *IEEE Photonics Technol. Lett.*, vol. 24, no. 13, pp. 1112–1114, Jul. 2012.

[38] S. A. Maas, *Microwave Mixers*, 2nd ed., Norwood, MA: Artech House, 1993.

[39] S. A. Maas, *Nonlinear Microwave and RF Circuits*, 2nd ed., Norwood, MA: Artech House, 2003.

[40] B. Mayer and R. Knoechel, “Biasable Balanced Mixers and Frequency Doublers using a New Planar Balun,” in *Proc. 20th European Microw. Conf.*, pp. 1027–1032, Sep. 1990.

[41] B. Heinemann, *et al.*, “High-performance BiCMOS technologies without epitaxially-buried subcollectors and deep trenches,” Semicond. Sci. Technol., vol. 22, no. 1, pp. S153–S157, Jan. 2007.

[42] Y. Shoji, K. Hamaguchi, and H. Ogawa, “A Low-Cost and Stable Millimeter-Wave Transmission System Using a Transmission-Filter-Less Double-Side-Band Millimeter-Wave Self-Heterodyne Transmission Technique,” *IEICE Trans. Commun.*, vol. E86-B, no. 6, pp. 1884–1892, Jun. 2003.

[43] M.-J. Lee, H. Rücker, and W.-Y. Choi, “Effects of Guard-Ring Structures on the Performance of Silicon Avalanche Photodetectors Fabricated With Standard CMOS Technology,” *IEEE Electron Device Lett.*, vol. 33, no. 1, pp. 80–82, Jan. 2012.

[44] J.-S. Youn *et al.*, “A 10-Gb/s 850-nm CMOS OEIC Receiver with a Silicon Avalanche Photodetector,” *IEEE J. Quantum Electron.*, vol. 48, pp. 229–236, Feb. 2012.

[45] G. S. Sahota and C. J. Persico, “High Dynamic Range Variable-Gain Amplifier for CDMA Wireless Applications,” in *ISSCC Dig. Tech. Papers*, pp. 374–375, 1997.

[46] K.-C. Choi *et al.*, “Demonstration of 60-GHz Link Using a 1.6-Gb/s Mixed-Mode BPSK Demodulator,” *IEICE Trans. Electron.*, vol. E93-C, pp. 1704–1707, Dec. 2010.

Publication lists

International Journals

[1] **Minsu Ko**, Jeong-Min Lee, Myung-Jae Lee, and Woo-Young Choi, "Low-Noise Design of 5-GHz CMOS Narrow-Band Photoreceiver with Integrated Silicon Avalanche Photodetector," *to be submitted to IEEE Trans. Microwave Theory Tech*.

[2] **Minsu Ko**, Myung-Jae Lee, Holger Rücker, and Woo-Young Choi, "Silicon photonics-wireless interface ICs for micro-/millimeter-wave fiber-wireless networks," *submitted to Optics Express*.

[3] **Minsu Ko**, Jin-Sung Youn, Myung-Jae Lee, Kwang-Chun Choi, Holger Rücker, and Woo-Young Choi, "Silicon Photonics-Wireless Interface IC for 60-GHz Wireless Link," *IEEE Photonics Technology Letters*, vol. 24, no.123, pp.1112-1114, Jul. 2012.

[4] **Minsu Ko**, Duho Kim, Holger Rücker, and Woo-Young Choi, "3-Gb/s 60-GHz Link With SiGe BiCMOS Receiver Front-End and CMOS Mixed-Mode QPSK Demodulator," *Journal of Semiconductor Technology and Science*, vol. 12, no. 4, pp. 256-261, Dec. 2011.

[5] **Minsu Ko**, Jae-Young Kim, Myung-Jae Lee, Holger Rücker, and Woo-Young Choi, "A Silicon Balanced Subharmonic Optoelectronic Mixer for 60-GHz Fiber-Wireless Downlink Application," IEEE Photonics Technology Letters, vol. 23, no. 23, pp.1805-1807, Dec. 2011.

[6] Duho Kim, **Minsu Ko**, Kwang-Chun Choi, and Woo-Young Choi, "Mixed-mode QPSK demodulator for home networking applications," IET Electronics Letters, vol. 47, issue 2, pp. 92-94, Jan. 2011.

[7] Kwang-Chun Choi, **Minsu Ko**, Duho Kim, and Woo-Young Choi, "Demonstration of 60-GHz Link Using a 1.6-Gb/s Mixed-mode BPSK Demodulator," IEICE Transactions on Electronics, vol.E93-C, pp.1704-1707, Dec. 2010.

International Conferences

[1] **Minsu Ko**, Jeong-Min Lee, Myung-Jae Lee, and Woo-Young Choi, "A 5-GHz CMOS Integrated Radio-Over-Fiber Receiver," *The 8th Asia-Pacific Microwave Photonics Conference*, Apr. 22-24, 2013, Gwangju, Korea.

[2] **Minsu Ko**, Myung-Jae Lee, Holger Rücker, and Woo-Young Choi, "Investigation of Optimal Silicon Avalanche Photodiode Pairs for 60-GHz Balanced Subharmonic Optoelectronic Mixers," *The 7th Asia-Pacific Microwave Photonics Conference*, Apr. 25-27, 2012, Kyoto, Japan.

[3] Duho Kim, **Minsu Ko**, Kwang-Chun Choi, and Woo-Young Choi, "A 4.8-Gb/s Mixed-mode CMOS QPSK Demodulator For 60-GHz Wireless Personal Area Networks," *IEEE Asia Pacific Conference on Circuits and Systems*, Dec. 6-9, 2010, Kuala Lumpur, Malaysia.

[4] **Minsu Ko**, Holger Rücker, and Woo-Young Choi, "A 53−64-GHz SiGe Up-Conversion Mixer with 4-GHz IF Bandwidth," *The 10th IEEE Topical Meeting on Silicon Monolithic Integrated Circuits in RF Systems*, Jan. 11-13, 2010, New Orleans, USA.

[5] Myung-Jae Lee, Jin-Sung Youn, Hyo-Soon Kang, Duho Kim, **Minsu Ko**, K.-Y. Park, and Woo-Young Choi, "622-Mb/s Downlink Transmission in a Fiber-Fed 60-GHz Wireless System Using a CMOS Integrated Optical Receiver," *IEEE International Topical Meeting on Microwave Photonics*, Oct. 14-16, 2009, Valencia, Spain.

[6] Kwang-Chun Choi, Duho Kim, **Minsu Ko**, and Woo-Young Choi, "1-Gb/s Mixed-mode BPSK Demodulator Using a Half-rate Linear Phase Detector for 60-GHz Wireless PAN Applications," *IEEE Asian Solid-State Circuits Conference*, Nov. 3-5, 2008, Fukuoka, Japan.

[7] **Minsu Ko**, Hyo-Soon Kang, and Woo-Young Choi, "A CMOS-Compatible Schottky-Barrier Diode Detector for 60-GHz Amplitude-Shift Keying (ASK) Systems," *IEEE MTT-S International Microwave Symposium*, Jun. 15-20, 2008, Atlanta, USA.

Domestic Conferences

[1] **Minsu Ko**, Jeong-Min Lee, Jin-Sung Youn, Myung-Jae Lee, and Woo-Young Choi, "SiGe BiCMOS Integrated Optical-to-Millimeter-Wave Converter for 60-GHz Fiber-Wireless Downlink," *The 19th Korean Conference on Semiconductors*, Feb. 15-17, 2012, Seoul, Korea.

[2] **Minsu Ko**, Duho Kim, Holger Rücker, and Woo-Young Choi, "3-Gb/s Radio Link With SiGe BiCMOS 60-GHz Receiver Front-End," *The 11th RF Integrated Circuit Technology Workshop*, Sep. 22-24, 2011, Jeju, Korea.

[3] **Minsu Ko**, Hyo-Soon Kang, and Woo-Young Choi, "0.18-um CMOS Schottky Barrier Diodes for 60-GHz Self-Heterodyne Systems," *Autumn Microwave & Radio Wave Conference*, Sep. 13-14, 2007, Jeju, Korea.

[4] **Minsu Ko**, Duho Kim, Jae-Young Kim, and Woo-Young Choi, "622-Mb/s Transmission in 60 GHz Using a Novel CMOS BPSK Demodulator," *Autumn Microwave & Radio Wave Conference*, Sep. 13-14, 2007, Jeju, Korea.

Awards

[1] **Best Student Poster Award**, "A 5-GHz CMOS Integrated Radio-Over-Fiber Receiver," *The 8th Asia-Pacific Microwave Photonics Conference*, Apr. 2013.

[2] **The 13th Korea Semiconductor Design Contest (Special Prize)**, "Photonics-Wireless Interface SoC for 60-GHz High-Speed Wireless Communications," *Korean Intellectual Property Office*, Dec. 2012.

[3] **Samsung Humantech Paper Award (Encouragement Prize)**, "A Novel Remote Access Point Based on a Multi-Functional CMOS-Compatible Silicon Avalanche Photodetector for Microwave/Millimeter-Wave Multi-Band Fiber-Wireless Systems, *Samsung Electronics Co., Ltd.*, Feb. 2012.

[4] **TMS Best Paper Award (Bronze Prize)**, "A Silicon Balanced Subharmonic Optoelectronic Mixer for 60-GHz Fiber-Wireless Downlink Application," *BK21 TMS Institute of Information Technology, School of Electrical and Electronic Engineering, Yonsei Univ., Seoul, Korea*, Jan. 2012.

[5] **Excellent International Conference Paper Award**, "1-Gb/s Mixed-Mode BPSK Demodulator Using a Half-Rate Linear Phase Detector for 60-GHz Wireless PAN Applications (Presented in IEEE Asian Solid-State Circuits Conference 2008)," *IC Design Education Center, Korea*, Oct. 2009.